Published in final edited form as:

Immunity. 2022 November 08; 55(11): 2006–2026.e6. doi:10.1016/j.immuni.2022.10.004.

The epigenetic state of IL-4-polarized macrophages enables inflammatory cistromic expansion and extended synergistic response to TLR ligands

Zsolt Czimmerer[1,2,11], **Laszlo Halasz**[3,12], **Bence Daniel**[3,11,12], **Zsofia Varga**[1], **Krisztian Bene**[1], **Apolka Domokos**[1,4], **Marten Hoeksema**[5], **Zeyang Shen**[5,6], **Wilhelm K. Berger**[3], **Timea Cseh**[1], **Karoly Jambrovics**[1], **Zsuzsanna Kolostyak**[1,4], **Ferenc Fenyvesi**[7], **Judit Varadi**[7], **Szilard Poliska**[1], **Gyorgy Hajas**[8,9], **Istvan Szatmari**[1], **Christopher K. Glass**[5,10], **Attila Bacsi**[8,9], **Laszlo Nagy**[1,3,13,*]

[1]Department of Biochemistry and Molecular Biology, Faculty of Medicine, University of Debrecen, Debrecen, Hungary

[2]Institute of Genetics, Biological Research Centre, Eötvös Loránd Research Network, Szeged, Hungary

[3]Departments of Medicine and Biological Chemistry, Johns Hopkins University School of Medicine, Institute for Fundamental Biomedical Research, Johns Hopkins All Children's Hospital, St. Petersburg, FL, USA

[4]Molecular Cell and Immunobiology Doctoral School, Faculty of Medicine, University of Debrecen 4032, Debrecen, Hungary

[5]Department of Cellular and Molecular Medicine, School of Medicine, University of California, San Diego, La Jolla, CA, USA

[6]Department of Bioengineering, Jacobs School of Engineering, University of California, San Diego, La Jolla, CA, USA

[7]Department of Pharmaceutical Technology, Faculty of Pharmacy, University of Debrecen, Debrecen, Hungary

[8]Department of Immunology, Faculty of Medicine, University of Debrecen, Debrecen, Hungary

[9]ELKH-DE Allergology Research Group, Debrecen, Hungary

*Correspondence: lnagy@jhmi.edu.

AUTHOR CONTRIBUTIONS

Z.C. and L.N. directed the study and wrote the manuscript. Z.C., B.D., Z.V., A.D., W.K.B., T.C., K.J., K.B., Z.K., F.F., J.V., S.P., G.H., I.S., and A.B. performed the experiments. L.H. designed the bioinformatic approaches and carried out the analyses. L.N. obtained funding and provided supervision. M.H., Z.S., and C.K.G. collaborated on the SNP analysis. All authors provided input into data analysis and approved the final version of the manuscript.

SUPPLEMENTAL INFORMATION

Supplemental information can be found online at https://doi.org/10.1016/j.immuni.2022.10.004.

DECLARATION OF INTERESTS

The authors declare no competing interests.

[10]Department of Medicine, School of Medicine, University of California, San Diego, La Jolla, CA, USA

[11]These authors contributed equally

[12]Present address: Stanford University School of Medicine, Department of Pathology, Stanford, CA, USA

[13]Lead contact

SUMMARY

Prior exposure to microenvironmental signals could fundamentally change the response of macrophages to subsequent stimuli. It is believed that T helper-2 (Th2)-cell-type cytokine interleukin-4 (IL-4) and Toll-like receptor (TLR) ligand-activated transcriptional programs mutually antagonize each other, and no remarkable convergence has been identified between them. In contrast, here, we show that IL-4-polarized macrophages established a hyperinflammatory gene expression program upon lipopolysaccharide (LPS) exposure. This phenomenon, which we termed extended synergy, was supported by IL-4-directed epigenomic remodeling, LPS-activated NF-κB-p65 cistrome expansion, and increased enhancer activity. The EGR2 transcription factor contributed to the extended synergy in a macrophage-subtype-specific manner. Consequently, the previously alternatively polarized macrophages produced increased amounts of immune-modulatory factors both *in vitro* and *in vivo* in a murine Th2 cell-type airway inflammation model upon LPS exposure. Our findings establish that IL-4-induced epigenetic reprogramming is responsible for the development of inflammatory hyperresponsiveness to TLR activation and contributes to lung pathologies.

Graphical Abstract

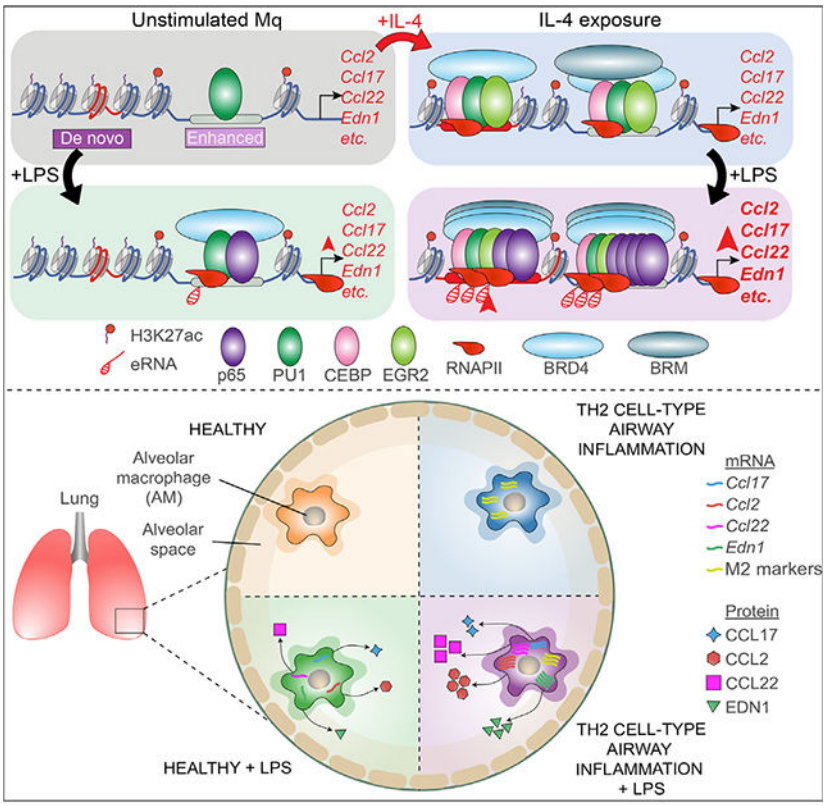

In brief

The antagonism between IL-4 and TLR ligands is expected and well described in macrophages, but their synergistic interactions are not understood. Czimmerer et al. demonstrate that IL-4-induced epigenetic reprogramming results in vast expansion of TLR-activated NF-κB-p65 cistrome, turning on a distinct hyperinflammatory gene expression program in murine and human macrophages.

INTRODUCTION

Features of macrophages (Macs) as well as their contribution to disease processes are determined by the tissue microenvironment, pathogen-derived molecules, and cytokines. Conventionally, the endpoints of cytokine-induced Mac activation states are T helper-1 (Th1) cell-type cytokine interferon-gamma (IFNγ)-induced classical (M(IFNγ)) and T helper-2 (Th2) cell-type cytokine interleukin 4 (IL-4)-mediated alternative (M(IL-4)) Mac polarization. M(IFNγ) Mac polarization programs are associated with inflammatory response, while M(IL-4)-type Macs protect against helminth infection and promote tissue regeneration. The classical and alternative Mac polarizing cytokines could be present simultaneously or sequentially in the microenvironment along with various pathogens or normal microbiota components and can lead to more nuanced, specialized Mac phenotypes and functions often associated with disease progression. Thus, the complex and changing milieu inevitably leads to heterogeneous polarization states *in vivo*, which are not well characterized (Gordon and Martinez, 2010; Murray et al., 2014; Murray and Wynn, 2011).

There are examples for enhanced inflammatory gene expression upon two distinct pro-inflammatory signaling events and blunting by anti-inflammatory cytokines. Activation of IFNγ--polarized Macs by Toll-like receptor (TLR) ligands leads to the so-called super-induction of many canonical inflammatory genes (Qiao et al. 2013). In addition, IFNγ prevents and reverses TLR ligands-induced Mac tolerance resulting in an exaggerated inflammatory phenotype in autoimmune diseases (Hu et al., 2008; Chen and Ivashkiv, 2010). Helminth infection-induced IL-4-dependent alternative Mac polarization markedly modifies the response against bacterial pathogens (Mylonas et al., 2009; Potian et al., 2011; Weng et al., 2007; Du Plessis et al., 2013). In addition, environmental lipopolysaccharide (LPS) contamination or expansion of particular Gram-negative bacteria in the bronchial airway microbiota exacerbates Th2 cell-type asthma (Eisenbarth et al., 2002; Goleva et al., 2013; Huang et al., 2011; Wang et al., 2021). The epigenomic basis of such interactions is not well understood.

The epigenomic and transcriptional programs of Mac polarization and inflammatory signal responses are tightly and dynamically regulated. First, lineage-determining transcription factors (LDTFs), including ETS domain, transcription factor PU.1, CCAAT-enhancer-binding proteins (C/EBPs), activator protein 1 (AP-1), or Runt-related transcription factor 1 (RUNX1), determine the Mac-specific-enhancer repertoire. Second, signal-dependent transcription factors (SDTFs), including IL-4- and IL-13-activated signal transducer and activator of transcription-6 (STAT6), IFNγ-activated STAT1, and LPS-activated nuclear factor kappa-light-chain-enhancer of activated B cells (NF-κB), or AP-1, are responsible for immediate-early transcriptional responses for Mac polarization and inflammatory signals (Glass and Natoli, 2016). Third, additional Mac-polarization-signal-induced or activated transcription factors such as IL-4-induced EGR2 or IFNγ-activated IRF1 and IRF8 also contribute to determining the late, stable epigenomic program of the differentially polarized Macs along with other transcription factors further downstream (Langlais et al., 2016; Daniel et al., 2020).

STAT1, STAT3, and IRF1 transcription factors contribute to the inflammatory hyper-responsiveness of IFNγ-primed Macs (Qiao et al. 2013; Kang et al., 2019). We recently found that the anti-inflammatory features of IL-4-primed Macs are based on the direct repressor activities of STAT6, affecting many TLR target genes (Czimmerer et al., 2018). Moreover, IL-4-enhanced inflammatory responsiveness has been also observed for certain genes, indicating that the effect of IL-4 on the TLR response is much more complex (Czimmerer et al., 2018; Major et al., 2002; Varin et al., 2010). This is clinically relevant because there are niches in the body, such as the lung, where a Th2 cell environment and pathogenic TLR activation may occur simultaneously and can lead to asthma exacerbation with glucocorticoid resistance (Eisenbarth et al., 2002; Goleva et al., 2013; Huang et al., 2011; Wang et al., 2021).

Here, we uncovered how IL-4 priming influences the epigenomic and transcriptomic outcomes of inflammatory responses in Macs. We identified a specific gene set displaying enhanced or *de novo* LPS responsiveness in IL-4-primed murine bone marrow-derived Macs (BMDMs). Enhanced LPS responsiveness was associated with IL-4-priming-dependent epigenomic reprogramming mediated by BRD4, as well as increased NF-κB-p65 binding

and enhancer activity. Finally, IL-4-facilitated LPS responsiveness (termed extended synergy) was found to be conserved between human and mouse Macs and regulated by transcription factors STAT6, NF-κB-p65, and EGR2 *ex vivo* in distinct murine tissue-resident and monocyte-derived murine Mac subsets and *in vivo* in alveolar Macs following the induction of Th2-type airway inflammation.

RESULTS

IL-4 priming followed by LPS activation induces a distinct cytokine and chemokine expression profile in murine Macs

We set out to study the LPS responsiveness of alternatively polarized Macs focusing first on the LPS-induced chemokine and cytokine signature. Using RNA-seq analysis, we found that 72 out of 229 genes from the “cytokine activity” gene ontology (GO) category (GO:0005125) showed LPS-induced mRNA expression in either non-polarized or alternatively polarized murine BMDMs or both. The LPS-dependent induction of many (14) chemokines and cytokines was significantly attenuated by IL-4 priming. However, another 29 chemokines and cytokines showed significantly enhanced LPS inducibility in IL-4 primed BMDMs (Figures 1A and S1A).

In order to investigate whether the modulating effects of IL-4 priming on LPS-induced cytokine and chemokine expression are restricted to TLR4 activation, we activated IL-4-primed and non-polarized BMDMs with ten different TLR agonists (Figure 1B). We measured the mRNA expression of five augmented and three attenuated LPS-inducible genes using RT-qPCR. Among the synergistically activated genes, *Ccl17* and *Ccl22* mRNA expression showed significantly elevated induction in IL-4-primed Macs upon each TLR agonist activation (Figure 1C). Although the increased responsiveness of the additional three selected genes in alternatively polarized Macs showed greater TLR ligand specificity, it was limited to the activation by TLR4 ligand on *Il23a* (Figure 1C). Similarly, IL-4-mediated repression was not restricted to TLR4 activation (Figure S1B).

NF-κB transcription factor complex mediates the response to TLR ligands; thus, we examined the activation of the NF-κB signaling in non-polarized and IL-4-primed BMDMs following LPS activation. Immunoblot data showed that IL-4 pre-treatment did not influence the LPS-mediated inhibitory IκBα protein degradation in wild-type (WT) and *Stat6*$^{-/-}$ BMDMs (Figure 1D). Immunoblot and fluorescence microscopy revealed that neither the expression nor the LPS-induced nuclear translocation of NF-κB-p65 was affected by IL-4 priming (Figures 1D–1F).

We asked whether NF-κB signaling was necessary for the enhanced gene-specific LPS responsiveness in IL-4-primed BMDMs. We studied the selected five genes in the presence of two NF-κB pathway inhibitors (BAY11–708 and Bot64). We found that the inhibitors attenuated the LPS-induced expression of the selected genes in both non-polarized and IL-4-primed murine BMDMs (Figure 1G).

Finally, we investigated whether IL-4 removal after 24 h of priming influences the ability of Macs to respond more robustly to LPS; thus, transcriptional memory developed. Therefore,

we measured LPS-induced mRNA expression of the selected five cytokines and chemokines without IL-4 washout and at different time points after washout (Figure S1C), As expected, IL-4-induced expression of alternative Mac polarization markers *Arg1* and *Chil3l3* returned to baseline within 24 h after the IL-4 washout (Figure S1D). In contrast, the elevated LPS responsiveness of *Ccl2*, *Il12a*, and *Il23a* was partially retained for a minimum of 24 h following IL-4 washout (Figure S1E), while the augmented LPS-mediated induction of *Ccl17*, and *Ccl22*, was not observed immediately after IL-4 washout or 24 h later (Figure S1E). However, the enhanced LPS responsiveness of *Ccl17* and *Ccl22* returned 48 and 72 h after the IL-4 washout (Figure S1D).

Therefore, IL-4 priming synergizes with TLR ligand activation that requires an intact NF-κB signaling but does not affect the nuclear translocation of NF-κB-p65. Moreover, there is gene-specific and continuous or intermittent time-limited transcriptional memory after IL4 exposure and thus the signals do not need to co-occur to induce extended synergy.

Prior IL-4 exposure approximately doubles the LPS-activated NF-κB-p65 cistrome, resulting in an altered enhancer landscape

Next, we investigated whether the enhanced LPS responsiveness of the previously identified cytokine and chemokine gene set was a consequence of IL-4 priming-modulated NF-κB-p65 binding and enhancer activation. Therefore, we first performed NF-κB-p65-specific chromatin immunoprecipitation followed by sequencing (ChIP-seq) in WT and *Stat6*$^{-/-}$ BMDMs (Figure S2A). Several differences were identified in the NF-κB-p65 cistrome between non-polarized and IL-4-primed WT Macs following 1-h LPS exposure (Figure S2B). IL-4 priming increased the number of NF-κB-p65 peaks from 25,428 to 48,507 (Figure 2A) and the occupancy of LPS-activated NF-κB-p65 at 26,440 genomic regions (Figure 2B; Table S1). In contrast, there was a significant reduction of NF-κB-p65 binding at only 1,545 genomic sites (Figure 2B; Table S1). Based on the presence or absence of NF-κB-p65 peaks in LPS-activated non-polarized Macs, the IL-4-facilitated NF-κB-p65-bound genomic regions could be divided into two groups. "*De novo*" NF-κB-p65 peaks could be detected at 15,236 genomic regions, while "enhanced" NF-κB-p65 binding could be found at an additional 11,204 regulatory regions (Figures 2C, 2E, and 2F). The IL-4 priming-induced NF-κB-p65 peak number and occupancy in LPS-activated alternatively polarized BMDMs proved to be strictly STAT6 dependent (Figures 2A, 2E, and 2F). The majority of genomic sites exhibiting IL-4-facilitated NF-κB-p65 binding were located in distal regulatory regions, including intergenic and intronic elements, with marginal differences between the different categories (Figure 2D).

To gain insight into the enhancer activity at the IL-4 priming-facilitated NF-κB-p65 binding-associated genomic sites, we examined the elongation-specific RNAPII-pS2 binding by ChIP-seq in LPS-exposed non-polarized and alternatively polarized Macs. 73% (11,166) of *de novo* and 94% (10,564) of enhanced NF-κB-p65 binding-associated genomic regions proved to be RNAPII-pS2 positive in at least one experimental condition (Figure S2C). K-means clustering of RNAPII-pS2-positive sites identified five clusters among both the *de novo* and the enhanced NF-κB-p65 peaks (Figure S2D). 42.9% of *de novo* and 49.9% of enhanced NF-κB-p65 binding-associated genomic regions showed maximal RNAPII-pS2

occupancy in the LPS-activated alternatively polarized BMDMs (Figure S2D). Among these genomic sites, 2,034 (18.2%) *de novo* and 1,831 (17.3%) enhanced NF-κB-p65 peaks (cluster I) were associated with RNAPII-pS2 enrichment in IL-4-primed Macs, which was further increased by LPS activation (Figures 2G and 2H). An additional 2,752 (24.6%) *de novo* and 3,444 (32.6%) enhanced NF-κB-p65-bound genomic regions (cluster II) showed LPS-induced RNAPII occupancy in non-polarized BMDMs. However, the LPS-induced RNAPII binding was significantly elevated in the IL-4-primed Macs (Figures 2G and 2H). The other three clusters were associated with IL-4 priming-attenuated (cluster III) or LPS-repressed (clusters IV and V) RNAPII-pS2 binding in the LPS-activated alternatively polarized Macs (Figures S2D–S2F).

These findings indicate that IL-4 priming induces the expansion of LPS-activated NF-κB-p65 cistrome resulting in a distinct active enhancer repertoire.

Increased NF-κB-p65 binding and enhancer activity supports the IL-4 and STAT6-dependent enhanced LPS responsiveness

To identify the gene sets affected by the LPS-induced NF-κB-p65 cistrome expansion and increased enhancer activation in alternatively polarized Macs, we performed RNA-seq in IL-4-primed and LPS-activated WT and *Stat6*$^{-/-}$ BMDMs. Our global transcriptome analysis demonstrated that the alternatively polarized WT BMDMs have a distinct LPS response compared with the WT non-polarized and IL-4-primed *Stat6*$^{-/-}$ Macs (Figure S3A). This distinct LPS response included extended synergy impacting the mRNA expression of 1,318 genes upon IL-4 priming and LPS activation (Figures 3A and S3B; Table S2). The elevated LPS response was strictly STAT6 dependent in IL-4-stimulated BMDMs (Figures 3A, S3A, and S3B). Based on the individual IL-4 and LPS responsiveness, the synergistically activated genes could be divided into nine clusters, of which four contained more than 90% of the genes (Figure 3B). 663 genes (50.30%) were induced by both IL-4 and LPS stimulation. 328 and 87 genes (24.88% and 6.60%) were activated by LPS or IL-4 alone, respectively. Finally, LPS-dependent activation of 141 genes (10.69%) was restricted to the IL-4-primed BMDMs, showing so-called *de novo* LPS responsiveness (Figure 3B). Next, we investigated RNAPII-pS2 binding at the gene bodies of genes induced by extended synergy using ChIP-seq. RNAPII-pS2 binding showed a similar pattern to the steady-state mRNA expression suggesting that prior IL-4 exposure enhances LPS-induced gene expression primarily at the transcriptional level (Figure S3C).

To determine the link between enhanced LPS responsiveness and *de novo* and enhanced NF-κB-p65-bound genomic regions, we assigned the regulatory elements from CI and CII clusters of *de novo* and enhanced NF-κB-p65 peak sets to the synergistically activated genes. We annotated 592 (cluster I) plus 910 (cluster II) *de novo* and 455 (CI) plus 933 (CII) enhanced NF-κB-p65 peaks falling into a ±100-kb genomic window around the transcription start site of the synergistically activated genes (Figures 3C–3E and S3D). 871 genes showed extended synergism and were associated with a minimum of one regulatory element exhibiting a *de novo* or enhanced pattern of NF-κB-p65 binding, while we could not assign such regulatory regions to the remaining 447 genes (Figure 3F). Based on the very high degree of enrichment of *de novo* or enhanced NF-κB-p65 peak in the examined gene loci,

we divided the *de novo* and/or enhanced NF-κB-p65 bound enhancer-associated genes into three categories. We identified 281 genes, among which more than 62.5% of the annotated synergistically activated and NF-κB-p65-positive enhancers belonged to the enhanced NF-κB-p65 binding-associated enhancer subset (Figure 3G; "dominantly enhanced" category). In contrast, 377 genes were associated with *de novo* NF-κB-p65 binding-linked enhancers in more than 62.5% (Figure 3G; "dominantly *de novo*" category). The remaining 213 genes were associated with *de novo* and enhanced NF-κB-p65 peaks of nearly 50–50 (Figure 3G, "both" category). During the characterization of the NF-κB-p65-mediated direct synergistic activation, we found that the number of regulatory regions annotated to highly synergistically activated genes showed that a remarkable portion of genes possessed only 1–2 enhanced and *de novo* NF-κB-p65-binding-associated regulatory elements. Additionally, the genes with a minimum of one *de novo* and enhanced NF-κB-p65 peak were associated with slightly more genomic regions with *de novo* NF-κB-p65 binding (Figure 3H).

To evaluate the identified three *de novo* and/or enhanced NF-κB-p65 peak-associated gene clusters, we performed GO biological process analysis using the Enrichr algorithm (Xie et al., 2021). We found that several immunologically relevant biological-process-associated gene sets were significantly enriched in each gene cluster, indicating that synergistic gene activation affects many aspects of the inflammatory and immunomodulatory functions of Macs. For instance, "monocyte chemotaxis" (GO:0002548) and "cytokine-mediated signaling pathway" (GO:0019221) GO biological process categories were enriched in the dominantlyenhancedNF-κB-p65-bound enhancers-associated gene cluster. Among others, the "neutrophil-mediated immunity" (GO:0002446) and "NIK-NF-κB signaling" (GO0038061) categories-linked genes were enriched in the dominantly *de novo* NF-κB-p65-bound enhancers-associated gene cluster, while the enrichment of the "inflammatory response" (GO:0006954) and "positive regulation of cytokine production" (GO:0001819) GO-terms-linked genes was observed in both *de novo* and enhanced NF-κB-p65 binding-associated gene clusters (Table S2), indicating that several aspects of inflammatory response and immunoregulation are affected by the extended synergy.

Next, we chose six representative genes associated with *de novo* and enhanced NF-κB-p65 peaks for further examination (Figures 3G, 3I, 3J, and S3E). In these cases, elevated RNAPII-pS2 binding was observed both on the gene bodies and at the NF-κB-p65-bound regulatory elements in alternatively polarized and LPS-activated BMDMs (Figures 3I and S3E), suggesting that the given enhancer(s) is(are) regulating the gene. To test this assumption, we measured the mRNA expression of these genes with RT-qPCR and confirmed their IL-4 priming-mediated and STAT6-dependent high-activation following LPS exposure (Figures 3J and S3F). In the case of three selected chemokines (CCL2, CCL17, and CCL22), we confirmed the significantly elevated protein secretion in IL-4-primed and LPS-activated WT BMDMs. In contrast, IL-4 priming failed to increase the LPS-induced secretion in the absence of STAT6 (Figure S3G), establishing a requirement of this factor.

Enhancer RNA (eRNA) expression is a proven and well-accepted surrogate for detecting and characterizing enhancer activity (Daniel et al., 2014; Natoli and Andrau, 2012). Therefore, we measured eRNA expression on three selected enhancers with elevated NF-κB-p65 and RNAPII-pS2 bindings in LPS-exposed alternatively polarized WT BMDMs. As expected,

IL-4 priming facilitated LPS-induced eRNA expression in a STAT6-dependent manner (Figure 3K).

Therefore, the distinct LPS responsiveness in alternatively polarized Macs is mediated, in large part, by elevated NF-κB-p65 binding and enhancer activity at their annotated regulatory regions of highly activated genes.

IL-4 priming facilitates NF-κB-p65 binding, and enhancer activity is preceded by increased chromatin accessibility and BRD4 binding

In order to investigate the epigenomic and chromatin level changes at the elevated NF-κB-p65 and RNAPII-pS2 co-bound regulatory elements of the synergistically activated genes, we assessed chromatin openness using the assay for transposase-accessible chromatin sequencing (ATAC-seq). We found that both *de novo* and enhanced NF-κB-p65-bound genomic regions showed weak ATAC-seq signals in the non-polarized state without LPS activation (Figures 4A, 4B, 4E, and S4A). IL-4 priming and LPS activation alone could induce chromatin opening, but maximal chromatin accessibility was observed in the alternatively polarized MACs following LPS activation (Figures 4A, 4B, 4E, and S4A). Thus, the elevated LPS-activated NF-κB-p65 binding and enhancer activity is linked to IL-4 priming-induced chromatin remodeling in alternatively polarized Macs, and most likely, it is required for that.

It has been demonstrated that bromodomain and extraterminal (BET) proteins, including BRD2 and BRD4, play an essential role in the LPS-induced gene and enhancer activation in Macs (Belkina et al., 2013; Hah et al., 2015). Therefore, we decided to examine whether the elevated NF-κB-p65 and RNAPII-pS2 co-binding are accompanied by enhanced BRD4 occupancy during the inflammatory response of alternatively polarized Macs. To do this, we assessed the genome-wide localization of BRD4. Cistrome analysis (ChIP-seq) unequivocally supported our hypothesis and showed that IL-4 priming and LPS activation-dependent BRD4 binding perfectly aligned with our RNAPII-pS2-specific ChIP-seq results at *de novo* and enhanced NF-κB-p65-bound genomic regions (Figures 4C–4E and S4A). These results raised the possibility that BRD4 is required for elevated LPS responsiveness in alternatively polarized Macs. To test the potential role of BET proteins, we aimed to examine the LPS-induced extended synergistic activation of the six previously selected genes in alternatively polarized BMDMs in the presence and the absence of BRD bromodomain inhibitor JQ1 (Figure S4B). The LPS-dependent induction was completely or partially inhibited in both non-polarized and alternatively polarized BMDMs except for *Ccl2* (Figures 4F and S4C). Similarly to the JQ1-dependent attenuation of extended synergistic activation of the mRNAs mentioned above, JQ1 could also inhibit the LPS-induced eRNA expression in IL-4-primed and control Macs at the previously selected distal regulatory regions except for *Ccl2*_−19Kb (Figures 4G and S4D).

These findings show that the IL-4-facilitated LPS responsiveness is accompanied by chromatin remodeling and requires BRD4 in most cases.

IL-4-induced EGR2 transcription factor is necessary for elevated LPS responsiveness in alternatively polarized Macs

In order to identify transcription factors participating in the elevated LPS responsiveness of alternatively polarized Macs, we performed transcription factor motif enrichment analysis at elevated NF-κB-p65 and RNAPII-pS2 co-bound genomic elements in the loci of synergistically activated genes. As expected, we could detect significant enrichment of Mac-specific various LDTF such as PU.1 and AP1, and the LPS-activated NF-κB-p65 binding motifs at both *de novo* and enhanced NF-κB-p65 binding-associated regulatory elements (Figure S5A). Additionally, the EGR binding motif was also significantly enriched at the examined NF-κB-p65 peak clusters except for cluster II from the enhanced NF-κB-p65 peak set, indicating that EGR transcription factors can play a pivotal role in the elevated inflammatory responsiveness of alternatively polarized Macs.

EGR2 transcription factor is an IL-4 inducible member of the EGR transcription factor family in Macs and is essential to establish and maintain the late, stable epigenomic program in alternatively polarized Macs (Daniel et al., 2020; Hoeksema et al., 2021). Therefore, we decided to study the contribution of EGR2 to the distinct LPS responsiveness of alternatively polarized Macs. First, we performed NF-κB-p65-specific ChIP-seq experiments in EGR2 deficient ($Egr2^{fl/fl}$) and control ($Egr2^{+/+}$) BMDMs to investigate whether EGR2 is necessary for the *de novo* and enhanced LPS-activated NF-κB-p65 binding in the alternatively polarized Macs. Both IL-4 priming-dependent *de novo* and enhanced NF-κB-p65 bindings were observed in $Egr2^{+/+}$ BMDMs following LPS activation, but IL-4 failed to facilitate NF-κB-p65 binding in the absence of EGR2 (Figures 5A and 5B). Next, we examined the LPS-induced high-activation at the gene expression level in IL-4-primed and non-polarized $Egr2^{+/+}$ and $Egr2^{fl/fl}$ BMDMs using RNA-seq. Our analysis revealed that the LPS response proved to be EGR2-independent in non-polarized Macs, while the LPS-induced high-activation was modified in the EGR2 deficient alternatively polarized Macs (Figure S5B). Specifically, the elevated LPS responsiveness of 469 genes was partially or entirely abolished in the IL-4-exposed EGR2 deficient Macs (Figure 5C; Table S3). In contrast, the mRNA expression of 16 genes was further increased in alternatively polarized $Egr2^{fl/fl}$ BMDMs following LPS activation (Figure S5C; Table S3). Four of the six previously characterized genes showed EGR2-dependent elevated LPS responsiveness in alternatively polarized Macs (Figure S5D). The LPS-induced secretion of the selected three chemokines showed a similar pattern to the mRNA expression. Specifically, EGR2 deficient alternatively polarized Macs secreted a significantly lower amount of CCL22, while their CCL2 and CCL17 secretion remained unchanged following LPS activation (Figure S5E).

We have recently described that EGR2 controls the late epigenetic program of alternative Mac polarization by direct and indirect mechanisms (Daniel et al., 2020). Therefore, we examined EGR2 binding at the distal regulatory regions of 469 highly activated genes, which showed attenuated LPS responsiveness in the EGR2 deficient IL-4 primed Macs. We classified these genes into three subgroups based on the binding of EGR2 to either *de novo* or enhanced NF-κB-p65-peak-associated regulatory regions. We found 226 genes, including *Il12a* and *Edn1*, with a minimum of one *de novo* or enhanced NF-κB-p65 peaks associated with IL-4-induced EGR2 binding (Figures 5D–5F). Most of these genes were also annotated

with *de novo* and enhanced NF-κB-p65 peaks, which did not overlap with EGR2 binding (Figures 5E and 5F). Additionally, 152 genes were associated with *de novo* or enhanced NF-κB-p65 binding at their regulatory regions without direct IL-4-induced EGR2 binding. The remaining 91 genes were not linked to *de novo* or enhanced NF-κB-p65 peaks using our criteria (Figure 5D).

Finally, we investigated the regulatory role of EGR2 in the elevated enhancer activation at two selected EGR2-bound enhancers, including *Il12a*_−57Kb, and *Edn1*_−9Kb (Figure 5F). RT-qPCR-based measurement of eRNA expression demonstrated that the IL-4 priming and LPS stimulation-dependent synergistic activation of both enhancers requires the presence of EGR2 in BMDMs (Figure 5G).

These results suggest that EGR2 contributes to the increased inflammatory responsiveness of alternatively polarized Macs and is required for many highly induced genes.

EGR2 binding to its response element is required for IL-4-induced epigenomic remodeling of the enhancers of highly activated genes

To investigate the direct contribution of the EGR2 transcription factor to the elevated LPS responsiveness of IL-4-primed Macs, we further studied the EGR2-bound *de novo* and enhanced NF-κB-p65 binding-associated regulatory regions. First, we analyzed the *de novo* EGR motif enrichment in these regions. According to the IL-4-induced EGR2 binding, the specific EGR binding motif was found at 94% of EGR2-bound regulatory regions, indicating the direct DNA binding of EGR2 at these genomic sites (Figures S6A and S6B).

Next, we investigated the effects of IL-4 priming on chromatin accessibility (by ATAC-seq), the enrichment of BRM (chromatin remodeling factor), PU.1 (LDTF), CEBPβ (LDTF), BRD4, RNAPII-pS2, and H3K27Ac at the EGR2-bound regulatory regions in WT and EGR2 deficient Macs. 24 h of IL-4 exposure led to elevated chromatin openness and BRM binding in an EGR2-dependent manner at the examined genomic regions (Figures 6A and 6B). Among the LDTFs, PU.1 binding was slightly induced, while CEBPβ binding was strongly induced by IL-4 priming in an EGR2-dependent fashion. Similarly, H3K27Ac, BRD4, and RNAPII-pS2 binding were induced in an IL-4 and EGR2-dependent manner (Figures 6A and 6B).

To provide further direct evidence that IL-4-induced EGR2 binding to specific DNA sequences is necessary for extreme synergism, we investigated the single nucleotide polymorphisms (SNPs) at the EGR2-bound enhancers in three different mouse lines, including C57BL/6J (C57), SPRET/EiJ (SPRET), and BALB/cJ (BALBc). We first trained a deep neural network model based on the *de novo* and enhanced NF-κB-p65 peaks within cluster I and II using a strategy as described previously (Hoeksema et al., 2021) and then used DeepLIFT (Shrikumar et al., 2017) to interpret the importance of single nucleotides. Top k-mers based on DeepLIFT scores correspond to previously identified motifs, including NF-κB, EGR, AP-1, etc. (Figure S5A; Table S4). As this deep learning model classifies *de novo* and enhanced peaks without specifically considering known transcription factor recognition motifs, the finding of these motifs within the top-ranked nucleotides provides an independent line of evidence for their functional importance.

SNPs overlaying with the top-ranked nucleotides are predicted to be functional. We detected 1–1 SNP at *Tmco3*_+6Kb, and *Btg1*_−10Kb enhancers in the SPRET mouse line, which were both predicted to be functional by DeepLIFT and decreased the affinity of the EGR binding motif. As measured by EGR2 ChIP-seq, the basal and IL-4-induced EGR2 binding was diminished at both enhancers in SPRET mice-derived BMDMs compared with the C57 and BALBc mice-derived Macs (Figure 6C). According to these findings, we observed the LPS-dependent *de novo* induction of *Btg1* and *Tmco3* expression in IL-4-primed WT C57 and BALBc mice-derived BMDMs, which was completely abolished in both EGR2 deficient C57 and SPRET mice-derived Macs (Figures 6D and 6E).

These findings support the conclusion that EGR2 contributes to the IL-4 priming-induced epigenomic reprogramming, mediating the enhanced LPS responsiveness of a set of genes in alternatively polarized Macs.

IL-4 priming and LPS-activation-induced extended synergy is present in murine-tissue-resident and human differentiating Macs

To broaden the scope of our studies we examined the IL-4 priming and LPS activation-induced gene expression changes in alveolar and large peritoneal Macs derived from embryonic precursors and thioglycolate-elicited small peritoneal Macs derived from blood monocytes (Ghosn et al., 2010; Epelman et al., 2014). Alternative Mac polarization markers *Chil3* and *Arg1* were induced in each Mac type by IL-4 (Figure S7A). By determining the mRNA expression of the six synergistically activated genes, we could observe elevated LPS responsiveness following the IL-4 priming in the studied Mac populations with minor Mac subtype-specific differences (Figure 7A). We concluded that extended synergy is not restricted to bone marrow and blood monocyte-derived Macs but can also be observed in distinct populations of embryonic precursor-derived tissue-resident Macs.

Next, we assessed human $CD14^+$ monocyte-derived differentiating Macs. We investigated the mRNA expression of the selected synergistically activated genes in human alternatively polarized Macs following LPS activation. As shown in Figure S7B, two genes, including IL12A and CCL22, showed elevated LPS responsiveness in the IL-4-primed human differentiating Macs indicating that the extended synergy is evolutionarily conserved.

Extended synergy operates in alveolar macs during allergic airway inflammation and drives enhanced LPS-induced inflammation

To determine whether the synergy between the alternative Mac polarizing and inflammatory signals is detectable *in vivo*, we studied a mouse model of alternative Mac polarization. Allergen-induced airway inflammation and asthma are associated with elevated Th2-type cytokine production, including IL-4 and alternative Mac polarization (Deng et al., 2019; Saradna et al., 2018; Robbe et al., 2015). We induced Th2-cell-type airway inflammation in sensitized animals using the clinically relevant ragweed pollen extract (RWE) challenge and characterized the dynamics of inflammation and alternative Mac polarization. As shown in Figure S7C, first, we sensitized the mice with two intraperitoneal RWE injections on days 0 and 4. Next, we induced Th2-cell-type airway inflammation with intranasal RWE treatment on day 11. We have characterized the developing Th2-cell-type inflammation, including *Il4*

and Th2 cell-type airway inflammation marker *Muc5ac* (Evans et al., 2015) RNA expression in total lung RNA extract and the immune cell composition of bronchoalveolar lavage fluids (BALFs), on day 11 before the RWE challenge (0 h) and 24 and 48 h after the RWE treatment. *Il4* and *Muc5ac* expression did not show any differences between RWE and PBS-sensitized mice-derived lung mRNA extracts at 0 h. Still, the intranasal RWE stimulation significantly induced them at both examined time points (Figures S7D and S7E). The immune cell composition of the BALFs has also dynamically changed following the intranasal RWE stimulation. Before the intranasal RWE challenge (at 0 h), we could not observe any differences in the immune cell composition of the PBS and RWE-exposed mice-derived BALFs, and the alveolar Mac was the dominant immune cell type in both experimental groups (Figure S7E). However, the intranasal RWE treatment induced the recruitment of neutrophil and eosinophil granulocytes with different dynamics (Figure S7F) (Hosoki et al., 2016). Finally, we examined the mRNA expression of the alternative Mac polarization markers *Arg1* and *Chil3* in F4/80 and CD11c double-positive alveolar Macs derived from our model system. Each alternative polarization marker was induced following the intranasal RWE stimulation and showed the highest expression at 48 h (Figure S7G).

Since alternative polarization of alveolar Macs is the most pronounced 48 h after intranasal RWE sensitization, we performed an LPS challenge intranasally at this time point, and isolated $F4/80^+$ and $CD11c^+$ alveolar Macs 6 h following treatment and studied synergistic gene activation *in vivo* (Figure 7B). We selected four synergistically activated genes for *in vivo* study of the identified phenomenon and measured their mRNA expression. In contrast to the *in vitro* results, the *Ccl17* mRNA expression was already induced in alveolar Macs from PBS-treated and LPS-exposed mice. However, the RWE challenge further enhanced the LPS-dependent induction of *Ccl17* (Figure 7C). In addition, *Ccl22*, *Ccl2*, and *Edn1* mRNA expression were slightly enhanced following PBS treatment by LPS, and their LPS responsiveness was markedly elevated in RWE-pretreated mice-derived alveolar Macs (Figure 7C). After that, we determined the secreted CCL17, CCL22, CCL2, and EDN1 protein amounts in BALFs derived from PBS or RWE-challenged mice following intranasal LPS stimulation. We could detect the same highly synergistic expression patterns in the secreted protein levels in each case (Figure 7D).

Elevated CCL2 expression in the lung leads to increased number of $CD11b^+$ exudative Macs in BALFs, contributing to the immune pathology in different infections and injuries (Lin et al., 2008; Winter et al., 2007; Liang et al., 2012). Thus, we decided to investigate whether RWE challenge-induced Th2-cell-type airway inflammation can influence the LPS-dependent increase of $CD11b^+$ exudative Mac content in BALFs. The exudative Mac content of the BALFs was negligible in the PBS and RWE-exposed mice, and its induction was observed 24 h after the intranasal LPS stimulation (Figure 7E). However, similarly to CCL2 production, the LPS-induced $CD11b^+$ exudative Mac content was significantly elevated in the BALF-derived RWE-challenged mice (Figure 7E), indicating that synergistic gene activation in alveolar Macs leads to LPS-induced immunopathology in the lung.

Looking at the physiological consequences of the interactions between the LPS-activated inflammatory and Th2-cell-type inflammatory pathways at the whole-body level, we found that LPS-induced transient body weight loss and hypothermia were significantly enhanced

in the RWE-challenged mice, indicating that Th2-cell-type airway inflammation exacerbated the LPS-induced inflammatory response (Figures 7F and 7G).

These findings indicate that the gene-specific enhanced LPS responsiveness of alternatively polarized Macs has pathophysiological consequences *in vivo* in a murine Th2 allergic airway inflammation model associated with elevated exudative Mac content in BALFs and exacerbated LPS-mediated inflammatory disease symptoms.

EGR2 regulates the synergistic activation of *Ccl2* expression in the alveolar Macs *ex vivo* and *in vivo*

Finally, clarified the role of EGR2 in regulating synergistic gene activation in alveolar Macs. We examined the IL-4-induced mRNA expression of canonical alternative Mac polarization markers *Chil3* and *Arg1 ex vivo* in alveolar Macs isolated from $Egr2^{+/+}$ *Lyz2-cre* and $Egr2^{fl/fl}$ *Lyz2-cre* mice. We found that the IL-4-dependent induction of *Chil3* mRNA expression was partially diminished in EGR2 deficient alveolar Macs (Figure S7H). In contrast, IL-4-induced *Arg1* expression was further enhanced in the $Egr2^{fl/fl}$ *Lyz2-cre* mice-derived alveolar Macs (Figure S7H), indicating the modified alternative polarization state in alveolar Macs in the absence of EGR2. Next, we wanted to investigate whether the IL-4 priming and LPS activation-mediated synergistic induction of *Ccl17*, *Ccl22*, *End1*, and *Ccl2* expression is EGR2 dependent in the alveolar Macs *ex vivo*. Synergistic induction of *Ccl2* was significantly increased in EGR2-deficient alveolar Macs, while the synergistic activation of the other three selected genes was not affected by the absence of EGR2 (Figure 7H). Finally, we examined the synergistic activation of *Ccl2* mRNA expression in sorted alveolar Macs and the secreted protein content in the bronchoalveolar lavage fluid samples from $Egr2^{fl/fl}$ *Lyz2-cre* mice (Figure 7B). Similarly to our *ex vivo* alveolar Mac-derived data, *in vivo* synergistic activation of *Ccl2* expression by RWE challenge and LPS treatment was significantly elevated at both mRNA expression and secreted protein levels in $Egr2^{fl/fl}$ *Lyz2-cre* mice compared with the control $Egr2^{+/+}$ *Lyz2-cre* animals (Figures 7I and 7J). Overall, we find that EGR2 is a major modulator of synergistic gene activation in alveolar Macs *ex vivo* and *in vivo*, but distinct from its observed role in murine BMDMs.

DISCUSSION

Understanding the nature of interactions between Mac polarization signals and pathogen-derived molecules is essential and will ultimately lead to exploitable insights into the development of differential immune responses and foster the development of novel therapeutic strategies. It is becoming clear that the innate immune responses of each individual are determined by (1) natural genetic variations (Fairfax et al., 2014; Lee et al., 2014) and (2) prior experience, disease state, and pathological or physiological exposures, including earlier infections or aging (DiNardo et al., 2021; Schultze and Aschenbrenner, 2021). Therefore, understanding the molecular underpinning of such interactions is critical not only at the organismal but also at the individual level. However, due to the complexity of the microenvironment, the molecular bases of these interactions are difficult, if not impossible to study *in vivo*.

Thus, we investigated the interactions between isolated signaling events at the epigenomic and transcriptomic levels *ex vivo* by utilizing murine BMDMs, and then, tissue-resident Macs. We unraveled a highly synergistic interaction between alternative Mac polarizing signal IL-4 and inflammatory signal LPS at the epigenomic and transcriptional levels. We have termed this phenomenon extended synergism for the following reasons: (1) the transcriptional output of LPS activation is 5 to 100 times larger for a distinct gene set in IL-4-primed Macs vs. non-polarized cells, (2) LPS-activated NF-κB-p65 cistrome is expanded with more than 15,000 new NF-κB-p65-bound genomic regions in IL-4-exposed Macs, (3) the enhanced gene activation is linked to the significant increment in enhancer activation, chromatin accessibility, and cofactor binding, and (4) some of the resulting secreted cytokine amounts are orders of magnitude higher than the ones produced by either signal alone. Importantly, extended synergism is present in all Mac subtypes we examined including human primary Macs and is induced by at least nine different TLR activators, in a gene-specific manner.

Here, we provided mechanistic insight into the IL-4 priming-enhanced gene subset-specific TLR4 response and the underlying IL-4-STAT6 signaling-directed epigenomic reprogramming. Integrative analysis of global transcriptional changes, chromatin structure, and NF-κB-p65 and RNAPII-pS2 cistromes showed that elevated inflammatory responsiveness is accompanied by the expansion of NF-κB-p65 cistrome, more accessible chromatin, and increased enhancer activation in alternatively polarized Macs. The identified highly activated genes and enhancers could be divided into two groups: (1) LPS activation was observed in non-polarized Macs, but IL-4 priming further enhanced it and (2) LPS responsiveness was only detected in the IL-4-exposed Macs, leading to *de novo* gene induction. The latter represented a qualitatively distinct biological response, similarly to our findings of repeated IL-4 exposure leading to the induction of a gene set not induced by the first stimulus (Daniel et al., 2018), illustrating the likely universality of the concept that repeated activating signals lead to the formation of an epigenomic memory and/or highly synergistic responses.

Despite some Mac subtype-, or TLR-ligand-specific differences, our observations held and revealed that this phenomenon is universal and is not restricted to the bone marrow and/or monocyte-derived Macs or TLR4 activation, and evolutionarily conserved. However, the transcriptional regulatory mechanisms leading to the extended synergism show distinct gene and/or Mac subtype-specific differences.

It appears that both STAT6 and NF-κB-p65 or to a lesser degree AP1 appear to be required components of extreme synergy at the enhancer selection and activation level. The role of EGR2 is more complex; (1) in BMDMs, IL-4-STAT6-induced EGR2 establishes and maintains the late, stable epigenomic and transcriptomic program of alternative Mac polarization (Daniel et al., 2020; Hoeksema et al., 2021); (2) however, *in vivo*, EGR2 is also required for the differentiation and specification of various tissue-resident Macs, including alveolar and $MHCII^{+}$ serous cavity Macs (Bain et al., 2022; McCowan et al., 2021). Here, we showed that EGR2 is an important but not exclusive regulator of extended synergism in different Mac subsets. EGR2 regulates different aspects of synergistic gene activation in alveolar Macs—both *ex vivo* and *in vivo*—if compared with BMDMs; synergistic induction

of *Ccl2* expression is EGR2-independent in BMDMs, while it restrains it in alveolar Macs in the context of Th2 cell-type inflammation superimposed with LPS exposure. These differences might be explained by the reported, different expression patterns and/or distinct roles of EGR2 in BMDMs versus alveolar Macs. While EGR2 is expressed only in IL-4 polarized cells and contributes to alternative polarization of BMDMs but not to their differentiation *per se* (Daniel et al., 2020), it is constitutively expressed in mature alveolar Macs and essential for their proper maturation and the maintenance of their homeostatic functions (McCowan et al., 2021). Therefore, we propose that this difference might account for the distinct expression patterns of regulated genes and regulatory roles of EGR2 in the extended synergy that we observed. Specifically, the altered basal state and pre-mature or incomplete phenotype in the EGR2 deficient alveolar Macs may result in enhanced synergistic activation of the inflammatory genes such as *Ccl2*, while the failure of the IL-4 induced epigenetic reprogramming in the absence of EGR2 leads to the abolished synergistic activation of a specific gene subset in BMDMs. In addition, other transcription factors may compensate for the lack of EGR2 in alveolar Macs in synergistic activation of the EGR2-dependent genes such as *Ccl22* and *Edn*1.

Regarding the requirement for co-stimulation and the existence of epigenetic memory in extended synergism, we investigated the LPS-induced elevated responsiveness in BMDMs at different time points after IL-4 washout. Similarly, as reported by van den Bossche and colleagues (van den Bossche et al., 2016), we showed that the 24 h resting period between the IL-4 priming and LPS activation does reduce the observed respective regulatory interaction but does not completely eliminate it for some genes. Additionally, two gene-specific phenomena could be observed regarding transcriptional memory: (1) for many genes, including *Ccl2* and *Il12a*, there is partially retained responsiveness; (2) for some genes, such as *Ccl22* and *Ccl17*, the responsiveness to synergistic gene activation returns at 72 h following IL-4 washout. In principle, both patterns prove that there is no absolute requirement for simultaneous or co-stimulation, broadening the biological and clinical relevance of the discovered phenomenon. The transient, refractory period is quite unusual, and likely to be linked to some yet unknown, intermittent signaling or epigenomic event. However, recent work on allergen-induced inflammation-driven TNF-dependent innate memory supports our finding and the likelihood of transcriptional memory for regulating *Ccl17* expression in Macs (Lechner et al., 2022).

The allergic asthma is accompanied by the elevated production of Th2 cell-type cytokines IL-4 and IL-13 and alternative Mac polarization although the pathological relevance of the alternatively polarized Macs is not completely understood (Lambrecht and Hammad, 2015; Abdelaziz et al., 2020). Th2 cell-type airway inflammation and asthma severity are influenced by the lung microbiome and pathogen infections. Several viral and bacterial infections or the expansion of specific Gram-negative bacteria in the airway microbiome can cause asthma exacerbation often combining with glucocorticoid resistance (Goleva et al., 2013; Huang et al., 2011; Busse et al., 2010; Johnston et al., 2006; Lieberman et al., 2003; Talbot et al., 2005), while it has also been described that asthma can sensitize to pneumonia (Zaidi and Blakey, 2019). Although the molecular basis of the complex interactions between the bacterial pathogens and the allergens-activated Th2-cell-type immune response is not fully understood, there is a growing recognition that bacterial infections in pre-existing

Th2-type inflammation can further potentiate Th2 cell-type inflammation and/or activate Th1 cell-type pathways resulting in a mixed immune activation and increased disease severity (Maltby et al., 2017). In line with these, we observed the development of complex inflammation as the consequence of the extended synergy; first, a wide range of immunomodulatory factors can be identified among the synergistically activated genes from the Th2-cell-mediated immune response-linked chemokines *Ccl17*, *Ccl22*, and *Ccl24* through the potent vasoconstrictor *Edn1* and the L-arginine transporter *Slc7a2* to the classical inflammation-associated genes including *Ccl2*, *Il6*, and *Nos2* in BMDMs; second, alveolar Macs also exhibit synergistic induction of *Ccl17*, *Ccl22*, *Ccl2*, and *Edn1* both *ex vivo* and *in vivo*. Finally, RWE-induced Th2-cell-type airway inflammation leads to exacerbated TLR4 activation-mediated inflammation, resulting in well-defined symptoms (e.g., loss of body weight and hypothermia) at the organismal level. Nevertheless, exploring the precise pathogenic role of the extended synergism in the development of the exacerbated inflammatory response in asthmatic mice requires further investigation.

Our work here provides insights into how IL-4 priming-induced epigenetic reprogramming leads to NF-κB-p65 cistrome expansion and gene and enhancer set-specific synergistic transcriptional activation in Macs following TLR4 activation. The described extreme synergy is inducible in Mac subtypes regardless of origin and by all TLR activation tested. Furthermore, the presented data raise the possibility that the alternatively polarized Macs have specific responsiveness to various pathogen-derived signals *in vitro* and *in vivo* that is not limited to the well-characterized transcriptional repression. The synergistically activated genes and resulting proteins but also the enhancers driving these processes can potentially be targeted to modulate alternative Mac polarization and TLR activation-associated complex pathological processes such as Th2 cell-mediated inflammation, severe asthma, or pneumonia.

Limitations of the study

In this study, we used murine BMDMs and alveolar Macs to study the extended synergism. The inherent difference between the epigenome of these two cell types, in particular, the distinct role EGR2 plays, necessitates future work to investigate the basis of the Mac subtype-specific action of EGR2 and also to characterize the pathological consequences of extended synergy *in vivo* in other models.

STAR★METHODS

RESOURCE AVAILABILITY

Lead contact—Further information and requests for resources and reagents should be directed to and will be fulfilled by the Lead Contact, Laszlo Nagy (lnagy@jhmi.edu).

Materials availability—This study did not generate new unique reagents.

Data and code availability—Sequencing data sets performed in this study are available at the NCBI GEO under accession numbers: GSE181223. Publicly available, published

ChIP-seq data sets can be accessed on the following GEO accession numbers: GSE159630 and GSE151015.

EXPERIMENTAL MODEL AND SUBJECT DETAILS

Mice—Female and male breeder mice for C57BL/6, BALBc and SPRET mice were used and bred under specific-pathogen-free (SPF) conditions. *Egr2*$^{fl/fl}$ *Lyz2-cre* and *Stat6*$^{-/-}$ animals were kept on the C57BL/6 genetic background. The *Egr2*$^{fl/fl}$ animals were a generous gift from Patrick Charnays laboratory. We crossed these animals with lysozyme-Cre (*Lyz2-cre*)+ animals to establish the conditional EGR2 deficient strain (*Egr2*$^{fl/fl}$ *Lyz2-cre*). These mice were backcrossed to the C57BL/6J strain for eight generations. As controls we used *Egr2*$^{+/+}$ *Lyz2-cre* littermates. Full-body *Stat6*$^{-/-}$ (Jackson Laboratory) animals were maintained by breeding STAT6 deficient male and female mice. WT C57BL/6 animals were used as controls. Animals were handled according to the regulatory standards of the animal facilities of the University of Debrecen, Johns Hopkins All Children's Hospital, and the University of California San Diego. Eight- to 12-week-old healthy female mice were used for all our experiments.

Bone marrow-derived macrophage differentiation and treatment conditions—Isolation and differentiation were completed as described earlier (Daniel et al., 2014). Isolated bone marrow-derived cells were differentiated for 6 days in the presence of L929 supernatant. Differentiated BMDMs were treated with IL-4 (20 ng/ml), LPS (100 ng/ml), PAM3CSK4 (100 ng/ml), HKLM (10^7/ml), polyI:C HMW (10 ug/ml), polyI:C LMW (10 ug/ml), FLA-ST (100 ng/ml), FSL-1 (100 ng/ml), ssRNA40 (1 ug/ml) and ODN1826 (5 uM) for the indicated period of time.

RWE sensitization and challenge—Six- to 8-week-old male C57/B6 WT mice were used for these studies. Allergic airway inflammation was induced with endotoxin-free ragweed pollen extract (RWE, Greer Laboratories) as we previously described (Boldogh et al., 2005) with some modification. Briefly, animals were sensitized with two intraperitoneal (i.p.) administrations (on days 0 and 4) of 300 μg RWE in calcium and magnesium free Dulbecco's phosphate-buffered saline (PBS, Sigma Chemical) injection combined in a 3 : 1 (75 μl : 25 μl) ratio with alum adjuvant (Thermo Fischer Scientific) or injected with the same volumes of PBS, as a vehicle control. On day 11, parallel groups of mice were challenged intranasally under ketamine and xylazine sedation with 240 μg RWE dissolved in 60 μl of phosphate-buffered saline or same volumes of PBS. On day 13, mice were challenged intranasally by 20 μg LPS (Salmonella enterica serotype minnesota Re 595-derived, Sigma-Aldrich) dissolved in 60 μl PBS or mice were challenged intranasally with same volumes of PBS. Animals were handled according to the regulatory standards of the animal facilities of the University of Debrecen. Animal studies were approved by the Animal Care and Protection Committee at the University of Debrecen (16/2019/DE MAB).

METHOD DETAILS

Real-time quantitative PCR for enhancer RNA and mRNA detection (qPCR)—RNA was isolated with Trizol reagent (Ambion). RNA was reverse transcribed with High-Capacity cDNA Reverse Transcription Kit (Applied Biosystems) according to

manufacturer's protocol. Transcript quantification was performed by qPCR reactions using SYBR green master mix (Roche). Transcript expressions were normalized to *Ppia*. Primer sequences are available in Table S5.

RNA-seq—The quality of total RNA samples was checked on Agilent BioAnalyzer using Eukaryotic Total RNA Nano Kit according to manufacturer's protocol. Samples with RNA integrity number (RIN) value >7 were accepted for library preparation process. RNA-Seq libraries were prepared from total RNA using Ultra II RNA Sample Prep kit (New England BioLabs) according to the manufacturer's protocol. Briefly, poly-A RNAs were captured by oligo-dT conjugated magnetic beads then the mRNAs were eluted and fragmented at 94-Celsius degree. First strand cDNA was generated by random priming reverse transcription and after second strand synthesis step double stranded cDNA was generated. After repairing ends, A-tailing and adapter ligation steps adapter ligated fragments were amplified in enrichment PCR and sequencing libraries were generated. Sequencing runs were executed on Illumina NextSeq 500 instrument using single-end 75 cycles sequencing.

ChIP-seq—ChIP was performed with minor modifications of the previously described protocol (Daniel et al., 2014). We lowered the sonication strength to low and shearing was performed in two consecutive rounds of 5 min (total 10 min). ChIP-Seq libraries were prepared by using Ovation Ultralow System V2 (Nugen Technologies) reagent kit according to manufacturer's protocol. Briefly, 1–5 ng of IP DNA sample was used for library preparation. End repair step was followed by A-tailing, adapter ligation and amplification steps. ChIP-Seq libraries were sequenced on Illumina NextSeq 500 instrument using single-end 75 cycles sequencing. The following antibodies were used: NFκB-p65 (sc-372), BRD4 (A301–985A100), RNAPII-pS2 (ab5095).

ATAC-seq—Macrophages were scraped and counted to achieve 60,000 cells per condition. Cells were washed in ice-cold PBS and nuclear isolation was performed in the following lysis buffer: 1% Triton-X-100, 0.1% SDS, 150 mM NaCl, 1 mM EDTA pH 8.0, and 20 mM Tris-HCl pH 8.0. Nuclei were subjected to tagmentation using Tn5 transposase at 37C for 30 minutes in the following reaction: 12.5 µl TD buffer, 10.5 µl H2O, and 2 µl Tn5 transposase (Illumina). Tagmentation was stopped by the addition of 75ul TE buffer and DNA was isolated with the Qiagen Minelute columns according to the manufacturer's protocol. Tagmented DNA was PCR amplified using Nextera primers, and the reaction clean-up was performed with AMPure XP beads by adding 90 µl beads to the 50 µl PCR reaction. Samples were subjected to Bioanalyzer fragment analysis and sequenced on the Illumina NextSeq 500 instrument.

Immunoblot—The collected cells were centrifuged at max RCF at 4°C for 15 minutes followed by the lysis of pellet in lysis buffer (50 mM TRIS, 1mM EDTA, 0.1 % MEA, 0,5% Triton X-100, 1 mM PMSF) containing a protease inhibitor cocktail (Sigma-Aldrich) with a 1:100x dilution ratio and sonicated with 4–5 strokes with 40% cycle intensity (Branson Sonifer, 450). The lysed cells were centrifuged at maximum rcf at 4°C for 15 min. The supernatant was collected for measurement of the protein concentration. The protein concentration was measured with the Pierce BCA Protein Assay Kit (Thermo Scientific) at

a wavelength of 570 nm (Thermo Multiskan Ascent). Every sample was measured with 3 technical parallels, normalized using BSA standard (Thermo Scientific, Stock: 2 mg/mL). The samples were diluted up to 2 mg/mL concentration, mixed with equal volumes of 23SDS denaturation-buffer (0.125 M Tris-HCl, pH 6.8, containing 4% SDS, 20% glycerol, 10% MEA, 0.02% bromophenol blue dye), and incubated at 99°C for 10 min.

Proteins were separated on 10 % SDS-polyacrylamide gels and blotted onto a PVDF membrane (MERCK-Millipore) using the semi-dry blotting method. Membranes were blocked with 5% non-fat dry milk or with 5% BSA in Tris-buffered saline and Tween 20 (TTBS) for 1 hour at room temperature. Primary antibodies were diluted in 0.5% milk or 5% BSA in 1xTTBS, with a dilution ratio of 1:1000–1:5000, incubated overnight at 4°C. The membranes were washed three times with 1xTTBS for 15 min at RT, incubated with horseradish peroxidase labelled secondary antibodies (Advansta) at a 1:10000–1:20000 dilution ratios for 1 hour at RT, followed by three times wash with 1xTTBS for 15 min at RT. The targeted protein bands were visualized using ECL-Kit (Advansta).

Fluorescence microscopy—For the investigation of nuclear translocation of NFκB-p65 800,000 BMDMs/well were seeded on round glass coverslips placed into 12 well plates. After the cells attached onto the coverslips, BMDMs were primed with IL-4 for 24 hours and activated with LPS for 1 1hour. Samples were washed twice with HBSS and fixed with methanol: acetone 1:1 for 10 min at room temperature, then cells were washed once with HBSS and incubated with FBS (Fetal Bovine Serum, Sigma) for 15 min at 37 °C to block the nonspecific binding sites. Cells were then rinsed with HBSS and incubated with 2 μg/ml primary anti-NFκB-p65 antibody (polyclonal rabbit IgG antibody, Santa Cruz Biotechnology Inc., Dallas, USA) for 1 h at 37 °C. After this incubation, cells were washed four times with HBSS and incubated with 5 μg/ml secondary antibody (Alexa Fluor 488 goat anti-rabbit IgG antibody, Invitrogen) for 1 h at 37 °C in the dark. Cells were washed four times again with HBSS and cell nuclei were stained with DAPI (283 nM) for 15 min at 37 °C. DAPI was removed from the samples by washing the specimens with HBSS and the round glass coverslips were glued onto microscope slides. Fluorescence microscopy measurements and analyses were carried out by a Zeiss Axioscope A1 (Jena, Germany) fluorescent microscope. The following filters were used to examine the samples: DAPI: excitation G 365 nm, emission BP 445/50 nm; fluorescein: excitation BP 470/40 nm, emission BP525/50 nm. The green fluorescence intensity of cell nuclei and cytosol were analysed by ZEN 2011 software (Zeiss, Jena, Germany) and the nuclear/cytosol intensity was calculated to express the extent of NFκB-p65 nuclear translocation.

Measurement of the body weight and temperature—24 hours after the last intranasal injection, measurements of the body temperature and the body weight of mice were started once a day for 6 or 7 days, respectively.

Bronchoalveolar lavage sample preparation—Bronchoalveolar lavage (BAL) was performed at 6 hours after the last intranasal challenge. To collect BAL samples, animals were euthanized, and their tracheas were cannulated. Lavage was performed with 2 aliquots of 0.7 ml of ice-cold PBS (pH 7.3). The BAL cells were centrifuged at 400 g for 10 minutes at 4 °C and the supernatants were removed and stored aliquoted at −80 °C for further

analysis. BAL cells were suspended in ACK buffer to lyse red blood cells for 2 minutes at room temperature and then adding 1 mL of MACS buffer. After washing step (at 800 rcf, 10 minutes, 4 °C), collected BAL cells were used for flow cytometry and cell sorting.

Peritoneal cell isolation—In respective experiments, 2.5% thioglycolate was injected 3 days prior to cell isolation. Mice were euthanized and peritoneal cells were collected by washing the peritoneum with 7 mL PBS. Collected cells were filtered using a 100 mm filter cap. After centrifugation (350×g, 5 minutes at 4oC) and red blood cell lyses was performed with 2 mL ACK buffer for 2 minutes at room temperature. After washing step with 10 mL PBS buffer, single cell suspensions in MACS buffer were prepared for flow cytometry and fluorescence-activated cell sorting (FACS).

Alveolar and peritoneal Mac isolation, flow cytometry, and cell sorting—BAL cells were labeled for anti-mouse CD11c-phycoerythrin ((PE), clone HL3, BD Biosciences) and anti-mouse F4/80-allophycocyanin ((APC), clone BM8, BioLegend) antibodies. Peritoneal cells were labelled for anti-mouse F4/80-APC and anti-mouse CD11b-PE-Cy7 (clone M1/70, eBioscience). The FcR Blocking Reagent (Miltenyi Biotec) was used to prevent non-specific bonding of antibody conjugates. To discriminate live and dead cells, the eBioscience™ Fixable Viability Dye eFluor™ 506 (Thermo Fischer Scientific) was used based on the manufacturer's recommendation. The CD11c-F4/80 double positive alveolar macrophages, F4/80loCD11blo small peritoneal macrophages, and F4/80hiCD11bhi large peritoneal macrophages were sorted by FACSAria™ III (BD Biosciences). Approximately 15,000–25,000 cells were separated for transcript analysis. The flow cytometry analysis and cell sorting were performed by BD FACSAria III (BD Biosciences) using BD FACSDiva Software 6.0 (BD Biosciences).

To determine total immune cell numbers of BAL samples, the CountBright™ Absolute Counting Beads (Thermo Fischer Scientific), Fc Receptor blocker (Miltenyi Biotec), anti-mouse F4/80-APC, anti-mouse CD11c-PE, and anti-mouse CD24-fluorescein-5-isothiocyanate (FITC) (clone M1/69, eBioscience) were used. The acquired flow cytometry data were analyzed with FlowJo v10.8 (BD Biosciences).

Cell counting—Total cell counts in BALF were determined from an aliquot of the cell suspension. Differential cell counts were performed on cyto-centrifuge preparations stained with eosin and thiazine (ELITech Biomedical Systems: Red Stain Reagent, Blue Stain, Rinse, Aerofix Additive).

Assessment of Muc5ac and IL-4 expression in the lungs—The mRNA expressions of Muc5ac and Il-4 were analyzed by RT-qPCR measurements. RNA was isolated from a frozen mouse lung tissue with Trizol reagent.

Ex vivo alveolar and peritoneal Mac polarization and activation—We cultured isolated cells at 24-well plates in a 0.5 mL RPMI medium containing 5% penicillin, 5% streptomycin, and 10% FBS. After attachment, we added 20 ng/ml IL-4 for 24 hours and then 100 ng/ml LPS for further 3 hours. total RNA was isolated by TRIZOL for mRNA transcripts detection.

Monocyte isolation and differentiation—Human monocytes were isolated from peripheral blood mononuclear cells (PBMC) of healthy volunteers. Buffy coats were obtained from the Regional Blood Bank.Monocyte separation was carried out using CD14 MicroBeads (Miltenyi Biotec) according to the manufacturer's instructions. Monocytes were cultured and differentiated to macrophages by their attachment to cell culture plate in RPMI 1640 supplemented with 10% FBS, 2 mM glutamine, penicillin and streptomycin for the indicated time (Daniel et al., 2020). Cells were pretreated with IL-4 (20 ng/ml) for 24 hours and activated by LPS (100 ng/ml) for 3 hours.

Enzyme-linked immunosorbent assay (ELISA)—Culture supernatants from cells were collected at the indicated times. Samples were centrifuged at 1000g for 10 min at 4°C, and the supernatants were separated and stored at −20°C until analysis. These cell culture and BAL supernatants were then probed for the presence of the following cytokine using ELISA kits according to the manufacturer's instructions: EDN1 (R&D Systems), CCL2/MCP-1 (BioLegend), CCL17/TARC (R&D Systems) and CCL22/MDC (R&D Systems). Plates were read using the BIO-TEK Synergy HT Multi-Detection Microplate Readermicroplate reader.

QUANTIFICATION AND DATA ANALYSIS

RNA-seq mapping and gene expression quantification—The single-ended mRNA sequence reads were analyzed using the nf-core/rnaseq v3.0 pipeline (Ewels et al., 2020). Sequencing quality was evaluated by *FastQC* software and reads were aligned to the *mm10* (GRCm38) genome assembly with *STAR* (Dobin et al., 2013) default parameters. Genes were quantified using *Salmon* (Patro et al., 2017). Genes with at least 10 Counts Per Million mapped read (CPM) were considered expressed. Multidimensional scaling (MDS) analysis was used to identify broad library-wise trends using the *cmdscale* function in R. Statistically significant difference was considered FDR < 0.1 from GLM test using R package *edgeR* (Robinson et al., 2010). Annotation of enhancers to differentially expressed genes was based on linear proximity (+/− 100 kilobase) to the transcription start sites (TSSs). Coverage profiles represent Reads Per Kilobase Million (RPKM) values, calculated using deeptools2 *bamCoverage* (Ramirez et al., 2016) and visualized in *IGV* (Robinson et al., 2011). Tables S2 and S3 contain the synergistically expressed genes with additional statistics.

ATAC-seq and ChIP-seq analyses—Sequencing quality was evaluated by *FastQC* software. The primary analysis of ATAC-seq was carried out using *nf-core/atacseq* pipeline. ChIP-seq read alignment and filtering were carried out using our ChIP-seq command line pipeline (Barta, 2011). Reads were mapped to the mouse reference genome (*mm10*) using the default parameters of *BWA MEM* aligner (Li and Durbin, 2009). Low mapping quality reads (MAPQ < 10), reads mapping to ENCODE mouse blacklisted regions (Amemiya et al., 2019) and duplicated reads were discarded from the downstream analyses, using *bedtools intersectBed* (Quinlan and Hall, 2010) and *samtools rmdup* (Li et al., 2009). MACS2 (Zhang et al., 2008) was used to call peaks at 5% false discovery rate (FDR). Coverage profiles represent Reads Per Kilobase Million (RPKM) values, calculated using deeptools2 *bamCoverage* (Ramirez et al., 2016) and visualized in IGV (Robinson et al., 2011). ATAC-seq and ChIP-seq read density profiles for region set summits were

calculated using deeptools2 *computeMatrix* (*-a 1500 -b 1500 -binSize 50*) and plotted with *plotHeatmap* function. Violin plots represents the mean RPKM of replicates. Genomic annotation of region sets was calculated using *HOMER* (Heinz et al., 2010) and plotted in R.

NFκB-p65 differential binding analysis—To determine differentially bound NFκB-p65 genomic regions, we first used *DiffBind* (Ross-Innes et al., 2012) to generate a consensus peak set with *minOverlap=2* for all samples. *DESeq2* (Love et al., 2014) was used to determine differentially bound sites at 10% false discovery rate (FDR). Library-wise similarities were determined using hierarchical clustering of the normalized values using the *hclust* function in R. ″*De novo*″ and ″enhanced″ NFκB-p65 sites were classified based on the presence of a called peak in the LPS-treated samples. IL-4 pretreatment facilitated NFκB-p65 sites (n=26440) were further classified based on their RNAPII activity patterns. For this, RNAPII reads were counted, low occupancy sites were removed and k-means clustering (k=5) was applied using *pheatmap* in R. Table S1 contains the detailed information for the NFkB-p65 consensus with additional statistics and annotation.

De novo motif analysis and motif enrichment—We used HOMER's *findMotifsGenome.pl* script to search for de novo motif enrichments with *mm10 -size given -dumpFasta -bits -homer2* parameters. The resulting EGR position weight matrices (PWMs) were used as an input for *annotatePeaks.pl* (*mm10 -size 1200 -hist 20*) to calculate motif enrichment scores and histograms. EGR motif occurrences in regions were calculated using *FIMO* (Grant et al., 2011) in R using the MEME Suite wrapper memes *runFimo* function with $p < 0.001$ cutoff. Data were visualized in R with *ggplot2*.

SNP analysis—To predict potential SNPs that alter enhancer functions, we trained a deep neural network model as described previously (Hoeksema et al., 2021). In brief, we adapted a strategy of *AgentBind* (Zheng et al., 2021) by fine-tuning a pre-trained DeepSEA model (Zhou and Troyanskaya, 2015) on all the ″*de novo*″ and ″enhanced″ NFκB-p65 peaks within Cluster I and II. Next, we used *DeepLIFT* (Shrikumar et al., 2017) to interpret the importance of single nucleotides. For each input sequence, we generated two sets of importance scores, one for the original sequence and the other for its reverse complement. The final *DeepLIFT* scores were displayed as the absolute maximum importance score at each aligned position. We defined top-scoring variants by their overlay with the top 20% (i.e., top 60) nucleotides of each 300-bp region. To interpret the important sequence patterns learned by neural networks, we computed the odds ratio of each 5-mer within the top 10% of all 5-mers (Zheng et al., 2021) and used Fisher's exact test to determine significant enrichment. For enriched 5-mers, we used TOMTOM (Gupta et al., 2007) to match with known transcription factor binding motifs from the JASPAR database (Fornes et al., 2020). The position weight matrix (PWM) of EGR2 motif was downloaded from JASPAR database with motif ID MA0472.1 (Fornes et al., 2020) and was used to compute motif score or PWM score and motif score difference between strain genomes. Motif matches were identified with a motif score cutoff at false positive rate < 0.1%.

Statistical analysis—Statistical analysis for qRT-PCR and ELISA methods: the error bars represent standard deviation (SD). The two-tailed Student's t test was used to evaluate

the significance of differences between two groups. Quantification and alignments of NGS analysis for RNA-seq, ChIP-seq, and ATAC-seq are also described in more detail in the methods section above.

Supplementary Material

Refer to Web version on PubMed Central for supplementary material.

ACKNOWLEDGMENTS

The authors would like to thank Aniko Nagy, Timea Gerzsenyi, Adel Lengyel, and Katalin Orosz-Toth for technical assistance and members of the Nagy laboratory for discussions and comments on the manuscript. Z.C. was supported by the Premium Postdoctoral Fellowship Program of the Hungarian Academy of Sciences, and L.N. was supported by the National Institutes of Health (R01DK115924 and DK124782). Support for this work in the Nuclear Receptor Research Laboratory was provided by the National Research, Development and Innovation Office (KKP129909 and FK132185 to Z.C.) and the European Union and the European Regional Development Fund (GINOP-2.3 2-15-2016-0006). A.B. was supported by the National Research, Development and Innovation Office (NKFIH K125337) and by GINOP-2.3.2-15-2016-00050 project. The project was co-financed by the European Union and the European Regional Development Fund. Z.V. was supported by the ÚNKP-20-4 New National Excellence Program of the Ministry for Innovation and Technology from the source of the National Research, Development and Innovation Fund.

REFERENCES

Abdelaziz MH, Abdelwahab SF, Wan J, Cai W, Huixuan W, Jianjun C, Kumar KD, Vasudevan A, Sadek A, Su Z, et al. (2020). Alternatively activated macrophages; a double-edged sword in allergic asthma. J. Transl. Med 18, 58. 10.1186/s12967-020-02251-w. [PubMed: 32024540]

Amemiya HM, Kundaje A, and Boyle AP (2019). The ENCODE blacklist : identification of problematic regions of the genome. Sci. Rep 9, 9354. 10.1038/s41598-019-45839-z. [PubMed: 31249361]

Bain CC, Louwe PA, Steers NJ, Bravo-Blas A, Hegarty LM, Pridans C, Milling SWF, MacDonald AS, Rückerl D, and Jenkins SJ (2022). CD11c identifies microbiota and EGR2-dependent MHCII + serous cavity macrophages with sexually dimorphic fate in mice. Eur. J. Immunol 52, 1243–1257. 10.1002/eji.202149756. [PubMed: 35568024]

Barta E (2011). Command line analysis of ChIP-seq results. EMBnet J. 17, 13–17.

Belkina AC, Nikolajczyk BS, and Denis GV (2013). BET protein function is required for inflammation: Brd2 genetic disruption and BET inhibitor JQ1 impair mouse macrophage inflammatory responses. J. Immunol 190, 3670–3678. 10.4049/jimmunol.1202838. [PubMed: 23420887]

Boldogh I, Bacsi A, Choudhury BK, Dharajiya N, Alam R, Hazra TK, Mitra S, Goldblum RM, and Sur S (2005). ROS generated by pollen NADPH oxidase provide a signal that augments antigen-induced allergic airway inflammation. J. Clin. Invest 115, 2169–2179. 10.1172/JCI24422. [PubMed: 16075057]

Busse WW, Lemanske RF, and Gern JE (2010). Role of viral respiratory infections in asthma and asthma exacerbations. Lancet 376, 826–834. 10.1016/S0140-6736(10)61380-3. [PubMed: 20816549]

Castro-Mondragon JA, Riudavets-Puig R, Rauluseviciute I, Berhanu Lemma R, Turchi L, Blanc-Mathieu R, et al. (2022). JASPAR 2022: the 9th release of the open-access database of transcription factor binding profiles. Nucleic Acids Res. 50 (D1), D165–D173. 10.1093/nar/gkab1113. [PubMed: 34850907]

Chen J, and Ivashkiv LB (2010). IFN-γ abrogates endotoxin tolerance by facilitating toll-like receptor-induced chromatin remodeling. Proc. Natl. Acad. Sci. USA 107, 19438–19443. 10.1073/pnas.1007816107. [PubMed: 20974955]

Czimmerer Z, Daniel B, Horvath A, Rückerl D, Nagy G, Kiss M, Peloquin M, Budai MM, Cuaranta-Monroy I, Simandi Z, et al. (2018). The transcription factor STAT6 mediates direct repression of

inflammatory enhancers and limits activation of alternatively polarized macrophages. Immunity 48. 75–90.e6. [PubMed: 29343442]

Daniel B, Czimmerer Z, Halasz L, Boto P, Kolostyak Z, Poliska S, Berger WK, Tzerpos P, Nagy G, Horvath A, et al. (2020). The transcription factor EGR2 is the molecular linchpin connecting STAT6 activation to the late, stable epigenomic program of alternative macrophage polarization. Genes Dev. 34, 1474–1492. 10.1101/gad.343038.120. [PubMed: 33060136]

Daniel B, Nagy G, Czimmerer Z, Horvath A, Hammers DW, Cuaranta-Monroy I, Poliska S, Tzerpos P, Kolostyak Z, Hays TT, et al. (2018). The nuclear receptor PPARγ controls progressive macrophage polarization as a ligand-insensitive epigenomic ratchet of transcriptional memory. Immunity 49. 615–626.e6. 10.1016/j.immuni.2018.09.005. [PubMed: 30332629]

Daniel B, Nagy G, Hah N, Horvath A, Czimmerer Z, Poliska S, Gyuris T, Keirsse J, Gysemans C, Van Ginderachter JA, et al. (2014). The active enhancer network operated by liganded RXR supports angiogenic activity in macrophages. Genes Dev. 28, 1562–1577. 10.1101/gad.242685.114. [PubMed: 25030696]

Deng R, Chen X, Zhang Y, Bian F, Gao N, Hu J, et al. (2019). Short ragweed pollen promotes M2 macrophage polarization via TSLP/TSLPR/OX40L signaling in allergic inflammation. 2019 Sep 1;12(5):1141–9. Mucosal Immunol. 12 (5), 1141–1149. 10.1038/s41385-019-0187-8. [PubMed: 31350466]

DiNardo AR, Netea MG, and Musher DM (2021). Postinfectious epigenetic immune modifications — a double-edged sword. N. Engl. J. Med 384, 261–270. 10.1056/NEJMra2028358. [PubMed: 33471978]

Dobin A, Davis CA, Schlesinger F, Drenkow J, Zaleski C, Jha S, Batut P, Chaisson M, and Gingeras TR (2013). STAR: ultrafast universal RNA-seq aligner. Bioinformatics 29, 15–21. 10.1093/bioinformatics/bts635. [PubMed: 23104886]

Du Plessis N, Kleynhans L, Thiart L, Van Helden PD, Brombacher F, Horsnell WGC, and Walzl G (2013). Acute helminth infection enhances early macrophage mediated control of mycobacterial infection. Mucosal Immunol. 6, 931–941. 10.1038/mi.2012.131. [PubMed: 23250274]

Eisenbarth SC, Piggott DA, Huleatt JW, Visintin I, Herrick CA, and Bottomly K (2002). Lipopolysaccharide-enhanced, toll-like receptor 4-dependent T helper cell type 2 responses to inhaled antigen. J. Exp. Med 196, 1645–1651. 10.1084/jem.20021340. [PubMed: 12486107]

Epelman S, Lavine KJ, and Randolph GJ (2014). Origin and functions of tissue macrophages. Immunity 41, 21–35. 10.1016/j.immuni.2014.06.013. [PubMed: 25035951]

Evans CM, Raclawska DS, Ttofali F, Liptzin DR, Fletcher AA, Harper DN, McGing MA, McElwee MM, Williams OW, Sanchez E, et al. (2015). The polymeric mucin Muc5ac is required for allergic airway hyperreactivity. Nat. Commun 6, 6281. 10.1038/ncomms7281. [PubMed: 25687754]

Ewels PA, Peltzer A, Fillinger S, Patel H, Alneberg J, Wilm A, Ulysse Garcia M, Di Tommaso P, and Nahnsen S (2020). The nf-core framework for community-curated bioinformatics pipelines. Nat. Biotechnol 38, 276–278. 10.1038/s41587-020-0435-1. [PubMed: 32055031]

Fairfax BP, Humburg P, Makino S, Naranbhai V, Wong D, Lau E, Jostins L, Plant K, Andrews R, McGee C, et al. (2014). Innate immune activity conditions the effect of regulatory variants upon monocyte gene expression. Science 343, 1246949. 10.1126/science.1246949. [PubMed: 24604202]

Fornes O, Castro-Mondragon JA, Khan A, Van Der Lee R, Zhang X, Richmond PA, Modi BP, Correard S, Gheorghe M, Baranašić D, et al. (2020). JASPAR 2020: update of the open-Access database of transcription factor binding profiles. Nucleic Acids Res. 48, D87–D92. 10.1093/nar/gkz1001. [PubMed: 31701148]

Ghosn EE, Cassado AA, Govoni GR, Fukuhara T, Yang Y, Monack DM, Bortoluci KR, Almeida SR, Herzenberg LA, and Herzenberg LA (2010). Two physically, functionally, and developmentally distinct peritoneal macrophage subsets. Proc. Natl. Acad. Sci. USA 107, 2568–2573. 10.1073/pnas.0915000107. [PubMed: 20133793]

Glass CK, and Natoli G (2016). Molecular control of activation and priming in macrophages. Nat. Immunol 17, 26–33. 10.1038/ni.3306. [PubMed: 26681459]

Goleva E, Jackson LP, Harris JK, Robertson CE, Sutherland ER, Hall CF, Good JT, Gelfand EW, Martin RJ, and Leung DYM (2013). The effects of airway microbiome on

corticosteroid responsiveness in asthma. Am. J. Respir. Crit. Care Med 188, 1193–1201. 10.1164/rccm.201304-0775OC. [PubMed: 24024497]

Gordon S, and Martinez FO (2010). Alternative activation of macrophages: mechanism and functions. Immunity 32, 593–604. 10.1016/j.immuni.2010.05.007. [PubMed: 20510870]

Grant CE, Bailey TL, and Noble WS (2011). FIMO : scanning for occurrences of a given motif. Bioinformatics 27, 1017–1018. 10.1093/bioinformatics/btr064. [PubMed: 21330290]

Gupta S, Stamatoyannopoulos JA, Bailey TL, and Noble WS (2007). Quantifying similarity between motifs. Genome Biol. 8, R24. 10.1186/gb-2007-8-2-r24. [PubMed: 17324271]

Hah N, Benner C, Chong LW, Yu RT, Downes M, and Evans RM (2015). Inflammation-sensitive super enhancers form domains of coordinately regulated enhancer RNAs. Proc. Natl. Acad. Sci. USA 112, E297–E302. 10.1073/pnas.1424028112. [PubMed: 25564661]

Heinz S, Benner C, Spann N, Bertolino E, Lin YC, Laslo P, Cheng JX, Murre C, Singh H, and Glass CK (2010). Simple combinations of lineage-determining transcription factors prime cis -regulatory elements required for macrophage and B cell identities. Mol. Cell 38, 576–589. 10.1016/j.molcel.2010.05.004. [PubMed: 20513432]

Hoeksema MA, Shen Z, Holtman IR, Zheng A, Spann NJ, Cobo I, Gymrek M, and Glass CK (2021). Mechanisms underlying divergent responses of genetically distinct macrophages to IL-4. Sci. Adv 7, 1–19. 10.1126/sciadv.abf9808.

Hosoki K, Aguilera-Aguirre L, Brasier AR, Kurosky A, Boldogh I, and Sur S (2016). Facilitation of allergic sensitization and allergic airway inflammation by pollen-induced innate neutrophil recruitment. Am. J. Respir. Cell Mol. Biol 54, 81–90. 10.1165/rcmb.2015-0044OC. [PubMed: 26086549]

Hu X, Chakravarty SD, and Ivashkiv LB (2008). Regulation of interferon and toll-like receptor signaling during macrophage activation by opposing feedforward and feedback inhibition mechanisms. Immunol. Rev 226, 41–56. 10.1111/j.1600-065X.2008.00707.x. [PubMed: 19161415]

Huang YJ, Nelson CE, Brodie EL, Desantis TZ, Baek MS, Liu J, Woyke T, Allgaier M, Bristow J, Wiener-Kronish JP, et al. (2011). Airway microbiota and bronchial hyperresponsiveness in patients with suboptimally controlled asthma. J. Allergy Clin. Immunol 127. 372–381.e1. 10.1016/j.jaci.2010.10.048. [PubMed: 21194740]

Johnston SL, Blasi F, Black PN, Martin RJ, Farrell DJ, and Nieman RB; TELICAST Investigators (2006). The effect of telithromycin in acute exacerbations of asthma. N. Engl. J. Med 354, 1589–1600. 10.1056/NEJMoa044080. [PubMed: 16611950]

Kang K, Bachu M, Park SH, Kang K, Bae S, Park-Min KH, and Ivashkiv LB (2019). IFN-γ selectively suppresses a subset of TLR4-activated genes and enhancers to potentiate macrophage activation. Nat. Commun 10, 3320. 10.1038/s41467-019-11147-3. [PubMed: 31346169]

Lambrecht BN, and Hammad H (2015). The immunology of asthma. Nat. Immunol 16, 45–56. 10.1038/ni.3049. [PubMed: 25521684]

Langlais D, Barreiro LB, and Gros P (2016). The macrophage IRF8/IRF1 regulome is required for protection against infections and is associated with chronic inflammation. J. Exp. Med 213, 585–603. 10.1084/jem.20151764. [PubMed: 27001747]

Lechner A, Henkel FDR, Hartung F, Bohnacker S, Alessandrini F, Gubernatorova EO, Drutskaya MS, Angioni C, Schreiber Y, Haimerl P, et al. (2022). Macrophages acquire a TNF-dependent inflammatory memory in allergic asthma. J. Allergy Clin. Immunol 149, 2078–2090. 10.1016/j.jaci.2021.11.026. [PubMed: 34974067]

Lee MN, Ye C, Villani AC, Raj T, Li W, Eisenhaure TM, Imboywa SH, Chipendo PI, Ran FA, Slowikowski K, et al. (2014). Common genetic variants modulate pathogen-sensing responses in human dendritic cells. Science 343, 1246980. 10.1126/science.1246980. [PubMed: 24604203]

Li H, and Durbin R (2009). Fast and accurate short read alignment with Burrows-Wheeler transform. Bioinformatics 25, 1754–1760. 10.1093/bioinformatics/btp324. [PubMed: 19451168]

Li H, Handsaker B, Wysoker A, Fennell T, Ruan J, Homer N, Marth G, Abecasis G, and Durbin R; 1000 Genome Project Data Processing Subgroup (2009). The Sequence Alignment / Map format and SAMtools. Bioinformatics 25, 2078–2079. 10.1093/bioinformatics/btp352. [PubMed: 19505943]

Liang J, Jung Y, Tighe RM, Xie T, Liu N, Leonard M, Dee Gunn M, Jiang D, and Noble PW (2012). A macrophage subpopulation recruited by CC chemokine ligand-2 clears apoptotic cells in noninfectious lung injury. Am. J. Physiol. Lung Cell. Mol. Physiol 302, L933–L940. 10.1152/ajplung.00256.2011.-CC. [PubMed: 22287613]

Lieberman D, Lieberman D, Printz S, Ben-Yaakov M, Lazarovich Z, Ohana B, Friedman MG, Dvoskin B, Leinonen M, and Boldur I (2003). Atypical pathogen infection in adults with acute exacerbation of bronchial asthma. Am. J. Respir. Crit. Care Med 167, 406–410. 10.1164/rccm.200209-996OC. [PubMed: 12426232]

Lin KL, Suzuki Y, Nakano H, Ramsburg E, and Gunn MD (2008). CCR2 + monocyte-derived dendritic cells and exudate macrophages produce influenza-induced pulmonary immune pathology and mortality. J. Immunol 180, 2562–2572. 10.4049/jimmunol.180.4.2562. [PubMed: 18250467]

Love MI, Huber W, and Anders S (2014). Moderated estimation of fold change and dispersion for RNA-seq data with DESeq2. Genome Biol. 15, 1–21. 10.1186/s13059-014-0550-8.

Major J, Fletcher JE, and Hamilton TA (2002). IL-4 pretreatment selectively enhances cytokine and chemokine production in lipopolysaccharide-stimulated mouse peritoneal macrophages. J. Immunol 168, 2456–2463. 10.4049/jimmunol.168.5.2456. [PubMed: 11859138]

Maltby S, Tay HL, Yang M, and Foster PS (2017). Mouse models of severe asthma: understanding the mechanisms of steroid resistance, tissue remodelling and disease exacerbation. Respirology 22, 874–885. 10.1111/resp.13052. [PubMed: 28401621]

McCowan J, Fercoq F, Kirkwood PM, T'Jonck W, Hegarty LM, Mawer CM, Cunningham R, Mirchandani AS, Hoy A, Humphries DC, et al. (2021). The transcription factor EGR2 is indispensable for tissue-specific imprinting of alveolar macrophages in health and tissue repair. Sci. Immunol 6, eabj2132. 10.1126/sciimmunol.abj2132. [PubMed: 34797692]

Murray PJ, Allen JE, Biswas SK, Fisher EA, Gilroy DW, Goerdt S, Gordon S, Hamilton JA, Ivashkiv LB, Lawrence T, et al. (2014). Macrophage activation and polarization: nomenclature and experimental guidelines. Immunity 41, 14–20. 10.1016/j.immuni.2014.06.008. [PubMed: 25035950]

Murray PJ, and Wynn TA (2011). Protective and pathogenic functions of macrophage subsets. Nat. Rev. Immunol 11, 723–737. 10.1038/nri3073. [PubMed: 21997792]

Mylonas KJ, Nair MG, Prieto-Lafuente L, Paape D, and Allen JE (2009). Alternatively activated macrophages elicited by helminth infection can be reprogrammed to enable microbial killing. J. Immunol 182, 3084–3094. 10.4049/jimmunol.0803463. [PubMed: 19234205]

Natoli G, and Andrau JC (2012). Noncoding transcription at enhancers: general principles and functional models. Annu. Rev. Genet 46, 1–19. 10.1146/annurev-genet-110711-155459. [PubMed: 22905871]

Patro R, Duggal G, Love MI, Irizarry RA, and Kingsford C (2017). Salmon provides fast and bias-aware quantification of transcript expression. Nat. Methods 14, 417–419. 10.1038/nmeth.4197. [PubMed: 28263959]

Potian JA, Rafi W, Bhatt K, McBride A, Gause WC, and Salgame P (2011). Preexisting helminth infection induces inhibition of innate pulmonary anti-tuberculosis defense by engaging the IL-4 receptor pathway. J. Exp. Med 208, 1863–1874. 10.1084/jem.20091473. [PubMed: 21825018]

Qiao Y, Giannopoulou EG, Chan CH, Park S-H, Gong S, Chen J, Hu X, Elemento O, and Ivashkiv LB (2013). Synergistic activation of inflammatory cytokine genes by interferon-g-induced chromatin remodeling and toll-like receptor signaling. Immunity 39, 454–469. 10.1016/j.immuni.2013.08.009. [PubMed: 24012417]

Quinlan AR, and Hall IM (2010). BEDTools : a flexible suite of utilities for comparing genomic features. Bioinformatics 26, 841–842. 10.1093/bioinformatics/btq033. [PubMed: 20110278]

R Core Team. (2020). R: A language and environment for statistical computing. R Foundation for Statistical Computing, Vienna, Austria. https://www.R-project.org/.

Ramirez F, Ryan DP, Bhardwaj V, Kilpert F, Richter AS, Heyne S, Friederike D, and Manke T (2016). deepTools2 : a next generation web server for deep-sequencing data analysis. Nucleic Acids Res. 44, 160–165. 10.1093/nar/gkw257.

Robbe P, Draijer C, Borg TR, Luinge M, Timens W, Wouters IM, Melgert BN, and Hylkema MN (2015). Distinct macrophage phenotypes in allergic and nonallergic lung inflammation. Am.

J. Physiol. Lung Cell. Mol. Physiol 308, L358–L367. 10.1152/ajplung.00341.2014. [PubMed: 25502502]

Robinson JT, Thorvaldsdóttir H, Winckler W, Guttman M, Lander ES, Getz G, and Mesirov JP (2011). Integrative genomics viewer. Nat. Biotechnol 29, 24–26. 10.1038/nbt.1754. [PubMed: 21221095]

Robinson MD, Mccarthy DJ, and Smyth GK (2010). edgeR : a Bioconductor package for differential expression analysis of digital gene expression data. Bioinformatics 26, 139–140. 10.1093/bioinformatics/btp616. [PubMed: 19910308]

Ross-Innes CS, Stark R, Teschendorff AE, Holmes KA, Ali HR, Dunning MJ, Brown GD, Gojis O, Ellis IO, Green AR, et al. (2012). Differential oestrogen receptor binding is associated with clinical outcome in breast cancer. Nature 481, 389–393. 10.1038/nature10730. [PubMed: 22217937]

Saradna A, Do DC, Kumar S, Fu QL, and Gao P (2018). Macrophage polarization and allergic asthma. Transl. Res 191, 1–14. 10.1016/j.trsl.2017.09.002. [PubMed: 29066321]

Schultze JL, and Aschenbrenner AC (2021). COVID-19 and the human innate immune system. Cell 184, 1671–1692. 10.1016/j.cell.2021.02.029. [PubMed: 33743212]

Shrikumar A, Greenside P, and Kundaje A (2017). Learning important features through propagating activation differences. Preprint at arXiv. 10.48550/arXiv.1704.02685.

Talbot TR, Hartert TV, Mitchel E, Halasa NB, Arbogast PG, Poehling KA, Schaffner W, Craig AS, and Griffin MR (2005). Asthma as a risk factor for invasive pneumococcal disease. N. Engl. J. Med 352, 2082–2090. 10.1056/NEJMoa044113. [PubMed: 15901861]

van den Bossche J, Baardman J, Otto NA, van der Velden S, Neele AE, van den Berg SM, Luque-Martin R, Chen HJ, Boshuizen MCS, Ahmed M, et al. (2016). Mitochondrial dysfunction prevents repolarization of inflammatory macrophages. Cell Rep. 17, 684–696. 10.1016/j.celrep.2016.09.008. [PubMed: 27732846]

Varin A, Mukhopadhyay S, Herbein G, and Gordon S (2010). Alternative activation of macrophages by IL-4 impairs phagocytosis of pathogens but potentiates microbial-induced signalling and cytokine secretion. Blood 115, 353–362. 10.1182/blood-2009-08-236711. [PubMed: 19880493]

Wang L, Netto KG, Zhou L, Liu X, Wang M, Zhang G, Foster PS, Li F, and Yang M (2021). Single-cell transcriptomic analysis reveals the immune landscape of lung in steroid-resistant asthma exacerbation. Proc. Natl. Acad. Sci. USA 118, 1–11. 10.1073/pnas.2005590118.

Weng M, Huntley D, Huang I-F, Foye-Jackson O, Wang L, Sarkissian A, Zhou Q, Walker WA, Cherayil BJ, and Shi HN (2007). Alternatively activated macrophages in intestinal helminth infection: effects on concurrent bacterial colitis. J. Immunol 179, 4721–4731. 10.4049/jimmunol.179.7.4721. [PubMed: 17878371]

Wickham H, Averick M, Bryan J, Chang W, McGowan LD, François R, et al. (2019). “Welcome to the tidyverse.”. Journal of Open Source Software 4 (43), 1686. 10.21105/joss.01686.

Winter C, Taut K, Srivastava M, Länger F, Mack M, Briles DE, Paton JC, Maus R, Welte T, Gunn MD, and Maus UA (2007). Lung-specific overexpression of CC chemokine ligand (CCL) 2 enhances the host defense to *Streptococcus pneumoniae* infection in mice: role of the CCL2-CCR2 axis. J. Immunol 178, 5828–5838. 10.4049/jimmunol.178.9.5828. [PubMed: 17442967]

Xie Z, Bailey A, Kuleshov MV, Clarke DJB, Evangelista JE, Jenkins SL, Lachmann A, Wojciechowicz ML, Kropiwnicki E, Jagodnik KM, et al. (2021). Gene set knowledge discovery with Enrichr. Curr. Protoc 1, e90. 10.1002/cpz1.90. [PubMed: 33780170]

Zaidi SR, and Blakey JD (2019). Why are people with asthma susceptible to pneumonia? A review of factors related to upper airway bacteria. Respirology 24, 423–430. 10.1111/resp.13528. [PubMed: 30887658]

Zhang Y, Liu T, Meyer CA, Eeckhoute J, Johnson DS, Bernstein BE, Nusbaum C, Myers RM, Brown M, Li W, and Liu XS (2008). Open access model-based analysis of ChIP-seq (MACS). Genome Biol. 9, R137. 10.1186/gb-2008-9-9-r137. [PubMed: 18798982]

Zheng A, Lamkin M, Zhao H, Wu C, Su H, and Gymrek M (2021). Deep neural networks identify sequence context features predictive of transcription factor binding. Nat. Mach. Intell 3, 172–180. 10.1038/s42256-020-00282-y. [PubMed: 33796819]

Zhou J, and Troyanskaya OG (2015). Predicting effects of noncoding variants with deep learning-based sequence model. Nat. Methods 12, 931–934. 10.1038/nmeth.3547. [PubMed: 26301843]

Highlights

- IL-4 priming leads to synergistic gene induction after TLR activation in macrophages
- IL-4 pre-treatment results in the expansion of NF-κB-p65 cistrome upon TLR activation
- EGR2 is a multi-faceted regulator of synergistic gene and enhancer activation
- Extended synergy is observed in a murine lung Th2-type inflammation model upon LPS

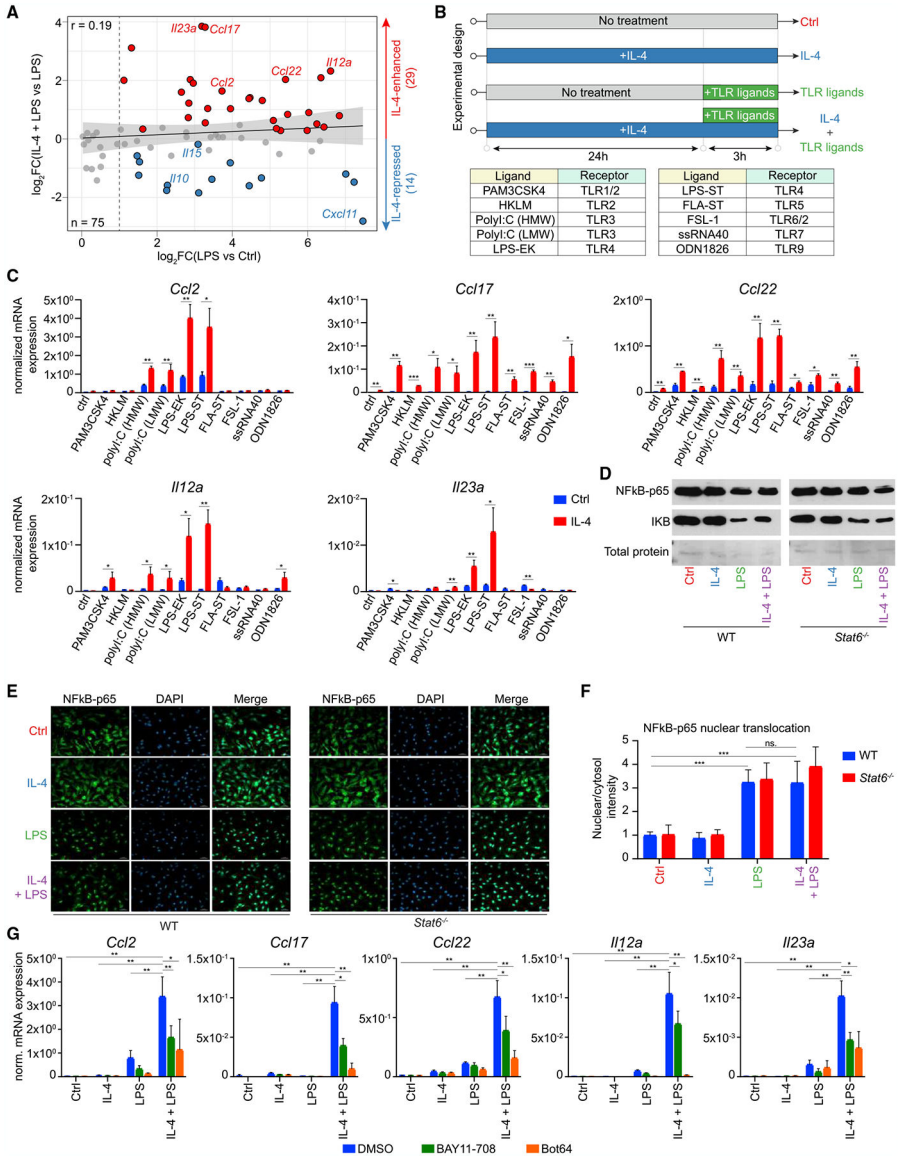

Figure 1. IL-4 priming followed by LPS activation induces a distinct cytokine and chemokine expression profile in murine Macs

(A) Dots plot visualization of RNA-seq fold changes of LPS-induced cytokines and chemokines in IL-4-primed and non-polarized WT BMDMs (n = 3). Colors indicate the sign of regulation in IL-4-primed BMDMs (edgeR; FDR < 10%).

(B) Experimental scheme for the gene expression experiments using various TLR ligands in IL-4-primed and non-polarized WT BMDMs.

(C) RT-qPCR measurements of the indicated cytokines and chemokines from IL-4-primed and non-polarized WT BMDMs following various TLR ligand activation (n = 4).

(D) Western blot of NF-κB-p65 and IκB expression in IL-4-primed and non-polarized WT and *Stat6*$^{-/-}$ BMDMs. One representative blot is shown from three independent experiments. Total protein serves as a loading control.

(E) Immunohistochemical staining and analysis of the nuclear factor kappa B (NF-κB) pathway activation in IL-4-primed and non-polarized WT and *Stat6*$^{-/-}$ BMDMs following

LPS stimulation. The nuclear localization of the NF-κB-p65 subunit was monitored by immunostaining. Green: p65 staining; blue: cell nuclei. Scale bars: 20 μm.

(F) The ratio of the fluorescence intensity of the NF-κB immunostaining in cell nuclei and cytosol was analyzed (n = 3 per genotype).

(G) RT-qPCR measurements on the indicated cytokines and chemokines from IL-4-primed and non-polarized WT BMDMs following LPS activation in the absence and presence of BAY11–708 or Bot64 NF-κB pathway inhibitors (n = 4).

WT bone marrow cells were isolated from mice with C57BL/6 genetic background. BMDMs were pretreated with IL-4 for 24 h (A and C–G) followed by LPS or other TLR ligand exposure for 1 h (D–F) or 3 h (A, C, and G).

Bar graphs present the mean ± SD of the biological replicates from two (C and G) or three (F) independent experiments. *$p < 0.05$, **$p < 0.01$, and ***$p < 0.001$, ns, not significant change.

See Figure S1.

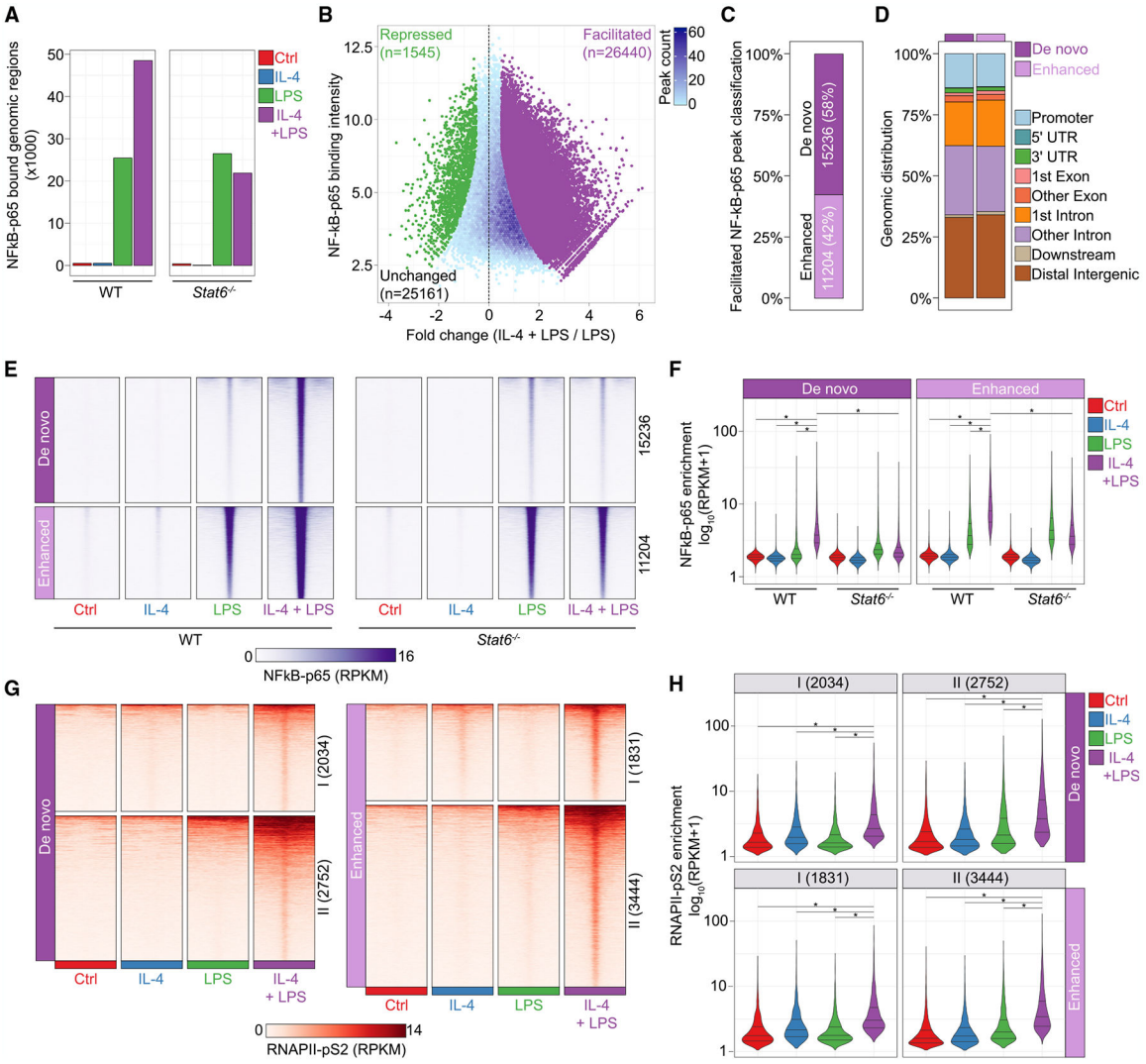

Figure 2. Prior IL-4 exposure facilitates the expansion of LPS-activated NF-κB-p65 cistrome, resulting in an altered enhancer landscape

(A) Bar plot visualization of the overall number of binding sites for NF-κB-p65 from ChIP-seq experiments in IL-4-primed and non-polarized WT and *Stat6*$^{-/-}$ BMDMs following LPS activation.

(B) Volcano plot visualization of LPS-activated NF-κB-p65 binding intensity in IL-4-primed and non-polarized WT BMDMs.

(C) Facilitated NF-κB-p65 peak classification based on the NF-κB-p65 binding in IL-4-primed BMDMs compared with non-polarized Macs.

(D) Genomic distribution of the regulatory elements exhibiting "*de novo*" and "enhanced" LPS-activated NF-κB-p65 binding in IL-4-primed WT BMDMs.

(E) Read distribution plot visualization of *de novo* and *enhanced* LPS-activated NF-κB-p65 binding in IL-4-primed WT and *Stat6*$^{-/-}$ BMDMs. Results are represented in RPKM (reads per kilobase per million mapped reads) values.

(F) Average binding signals for NF-κB-p65 are represented as violin plots on the genomic regions showing *de novo* and enhanced LPS-activated NF-κB-p65 binding in IL-4-primed WT BMDMs.
(G) Read distribution plot visualization of RNAPII-pS2 occupancy at the synergistically activated *de novo* and enhanced NF-κB-p65 binding-associated regulatory regions in IL-4-primed and LPS-exposed BMDMs. Results are represented in RPKM values.
(H) Average binding signals for RNAPII-pS2 are represented as violin plots on the genomic regions showing synergistic activation at *de novo* and *enhanced* NF-κB-p65-binding-associated genomic regions in IL-4-primed and LPS-exposed WT BMDMs.
WT and Stat6$^{-/-}$ bone marrow cells were isolated from mice with C57BL/6 genetic background. BMDMs were pretreated with IL-4 for 24 h followed by LPS exposure for 1 h (A–H). Data in (A)–(H) are combined from two independent biological replicates. Average $\log_{10}$ RPKM values are plotted. Significant changes are determined with the Wilcoxon test at $p < 0.01$ (F and H).
See Figure S2.

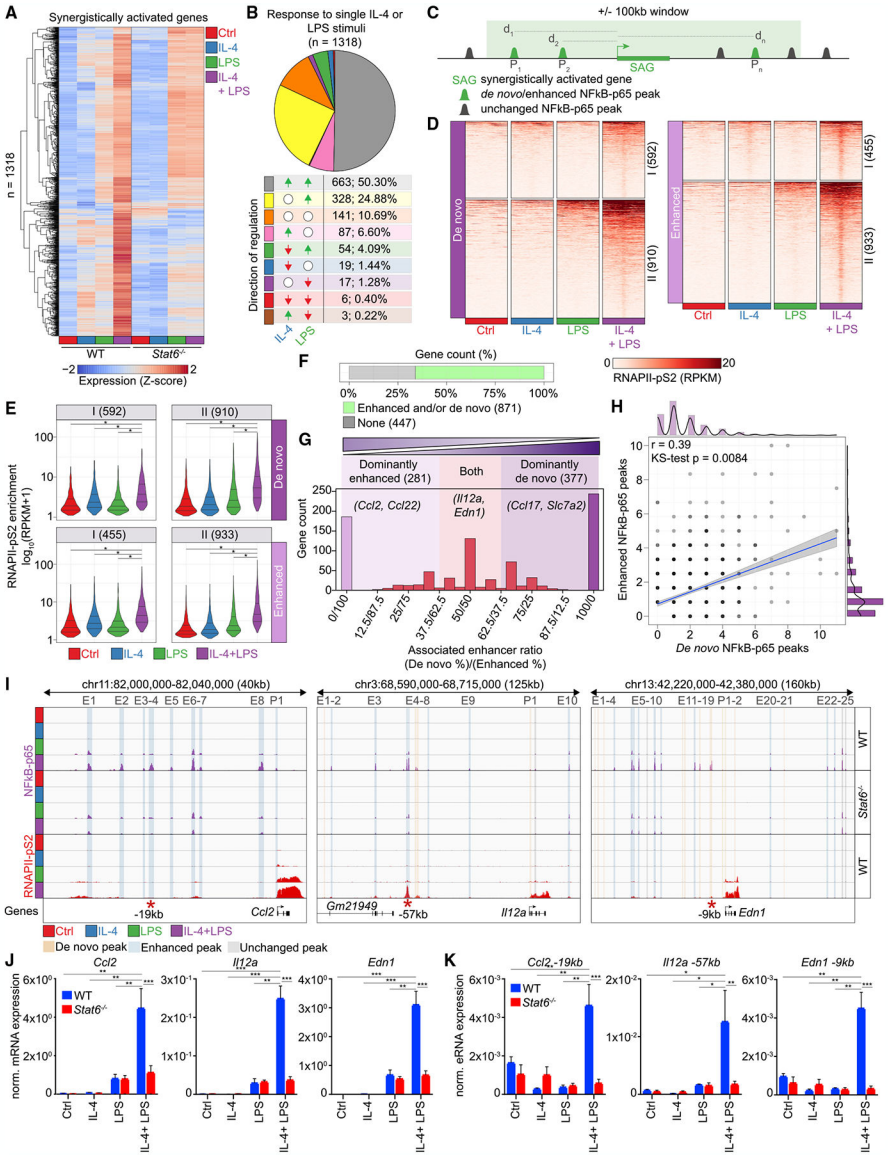

Figure 3. Increased NF-κB-p65 binding and enhancer activity supports the IL-4-STAT6-dependent enhanced LPS responsiveness

(A) Heatmap representation of synergistically activated genes in IL-4-primed and LPS-exposed WT (n = 3) and *Stat6*$^{-/-}$ (n = 3) BMDMs.

(B) Classification of the synergistically activated genes based on their responsiveness to LPS and IL-4 stimuli. The green arrow indicates significant up-regulation, the red arrow indicates significant down-regulation, and the empty circle indicates the lack of significant differences compared with non-polarized Macs.

(C) Scheme for annotating the synergistically activated *de novo* and enhanced LPS-activated NF-κB-p65 binding-associated regulatory regions to the synergistically activated genes.

(D) Read distribution plot visualization of RNAPII-pS2 occupancy at the annotated synergistically activated *de novo* and enhanced NF-κB-p65 binding-associated regulatory regions in IL-4-primed and LPS-exposed-BMDMs. Results are represented in RPKM values.

(E) Average binding signals for RNAPII-pS2 are represented as violin plots on the genomic regions showing synergistic activation at *de novo* and enhanced NF-κB-p65-binding-associated genomic regions in IL-4-primed and LPS-exposed WT BMDMs. Average $\log_{10}$ RPKM values are plotted. Significant changes are determined with the Wilcoxon test at $p < 0.01$.

(F) Classification of synergistically activated genes based on the annotated number of regulatory regions exhibiting *de novo* or enhanced NF-κB-p65 binding with elevated LPS-induced genome activity in IL-4-primed Macs. Gene counts for each bar are represented, and the circles below indicate the presence or absence of annotated regulatory elements from the different enhancer groups. Percentage-wise distribution of the synergistically activated genes with enhancer regions of the indicated NF-κB-p65 binding patterns (stacked bar plot at the right).

(G) Classification of *de novo* and/or enhanced NF-κB-p65 bound enhancer-associated synergistically activated genes based on the *de novo* or enhanced NF-κB-p65 peak dominancy in the examined gene loci. The number of genes and the representative examples are sown in each category.

(H) *De novo* or enhanced NF-κB-p65 binding-associated regulatory regions showing elevated LPS responsiveness in IL-4-primed BMDMs are annotated to synergistically activated genes. The number of regulatory elements annotated to the genes and their ratio to each other are shown.

(I) Genome browser view on the *Ccl2*, *Il12a*, and *Edn1* loci. ChIP-seq results for NF-κB-p65 in WT and *Stat6*$^{-/-}$ BMDMs and RNAPII-pS2 in WT Macs are shown. IL-4-primed and non-polarized Macs with or without LPS exposure are depicted for each protein.

(J) RT-qPCR measurements on the indicated synergistically activated genes from IL-4-primed and non-polarized WT and *Stat6*$^{-/-}$ BMDMs following LPS exposure (n = 4–5 per genotype).

(K) RT-qPCR measurements of eRNA expression at the selected synergistically activated enhancers from IL-4-primed and non-polarized WT and *Stat6*$^{-/-}$ BMDMs following LPS exposure (n = 4–5 per genotype).

WT and Stat6$^{-/-}$ bone marrow cells were isolated from mice with C57BL/6 genetic background. BMDMs were pretreated with IL-4 for 24 h followed by LPS exposure for 1 h (D–H) or for 3 h (A, B, J, and K). Data in (D)–(H) are combined from two independent biological replicates.

Bar graphs present the mean ± SD of the biological replicates from two independent experiments (J and K). *$p < 0.05$, **$p < 0.01$, ***$p < 0.001$, ns, not significant change. See Figure S3.

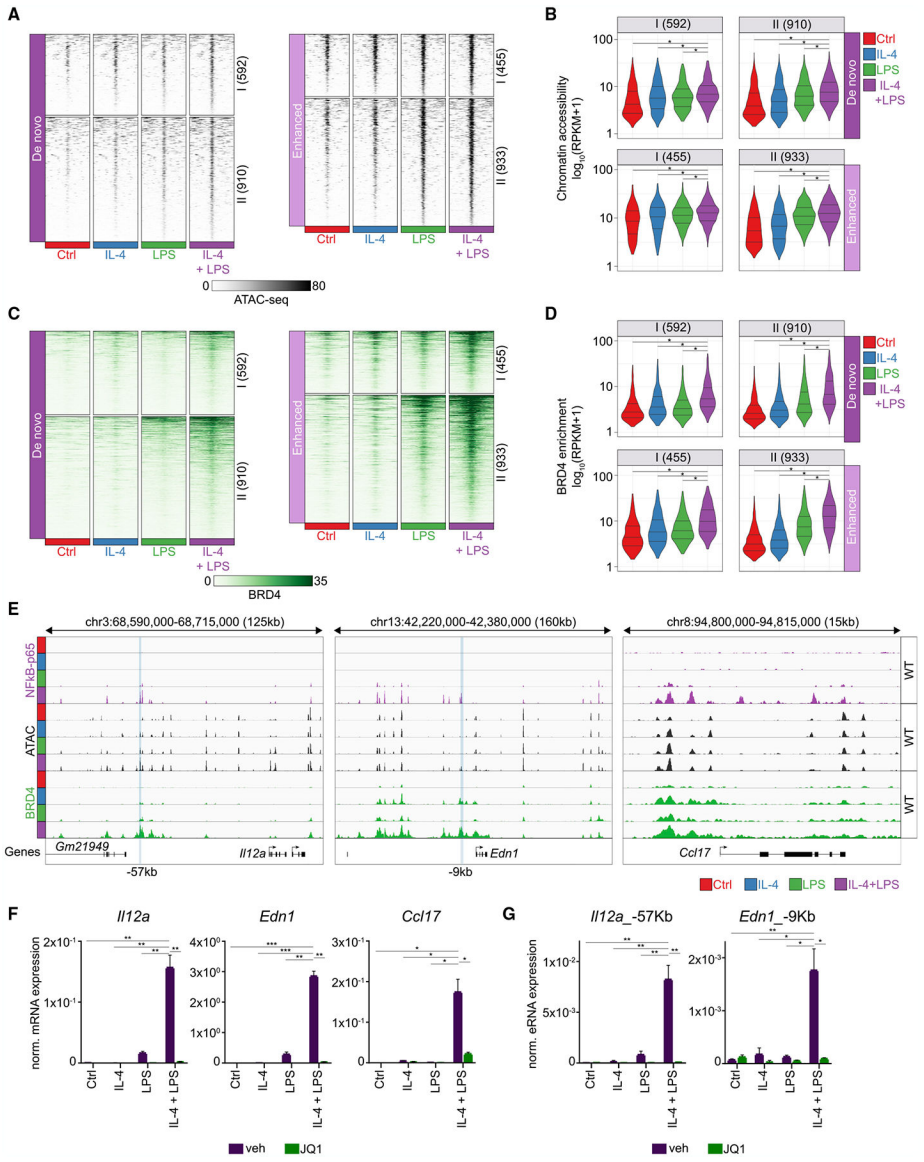

Figure 4. The IL-4 priming-facilitated NF-κB-p65 binding and enhancer activity is preceded by increased chromatin accessibility and BRD4 binding

(A) Read distribution plot visualization of the ATAC-seq signal at the annotated synergistically activated *de novo* and enhanced NF-κB-p65 binding-associated regulatory regions in IL-4-primed and LPS-exposed BMDMs. Results are represented in RPKM values.

(B) Average ATAC-seq signals are represented as violin plots on the genomic regions showing synergistic activation at *de novo* and enhanced NF-κB-p65 binding-associated genomic regions in IL-4-primed and LPS-exposed WT BMDMs.

(C) Read distribution plot visualization of BRD4 binding at the annotated synergistically activated *de novo* and enhanced NF-κB-p65 binding-associated regulatory regions in IL-4-primed and LPS-exposed BMDMs. Results are represented in RPKM values.

(D) Average binding signals for BRD4 are represented as violin plots on the genomic regions showing synergistic activation at *de novo* and enhanced NF-κB-p65 binding-associated genomic regions in IL-4-primed and LPS-exposed WT BMDMs.

(E) Genome browser view on the *Ccl2*, *Il12a*, and *Edn1* loci. ChIP-seq results for NF-κB-p65 and BRD4 and ATAC-seq results in WT Macs are shown. IL-4-primed and non-polarized Macs with or without LPS exposure are depicted for both ChIP-seq and ATAC-seq methods.

(F) RT-qPCR measurements on the indicated synergistically activated genes from IL-4-primed and non-polarized WT BMDMs following LPS exposure in the absence and presence of BRD inhibitor JQ1 (n = 3).

(G) RT-qPCR measurements of eRNA expression at the selected synergistically activated enhancers from IL-4-primed and non-polarized WT BMDMs following LPS exposure in the absence and presence of BRD inhibitor JQ1 (n = 3).

WT bone marrow cells were isolated from mice with C57BL/6 genetic background. BMDMs were pretreated with IL-4 for 24 h followed by LPS exposure for 1 h (A–E) or for 3 h (F and G). Data in (A)–(D) are combined from two independent biological replicates. Average $\log_{10}$ RPKM values are plotted. Significant changes are determined with the Wilcoxon test at $p < 0.01$ (B and D).

Bar graphs present the mean ± SD of the biological replicates. *$p < 0.05$, **$p < 0.01$, ***$p < 0.001$, ns, not significant change (F and G).

See Figure S4.

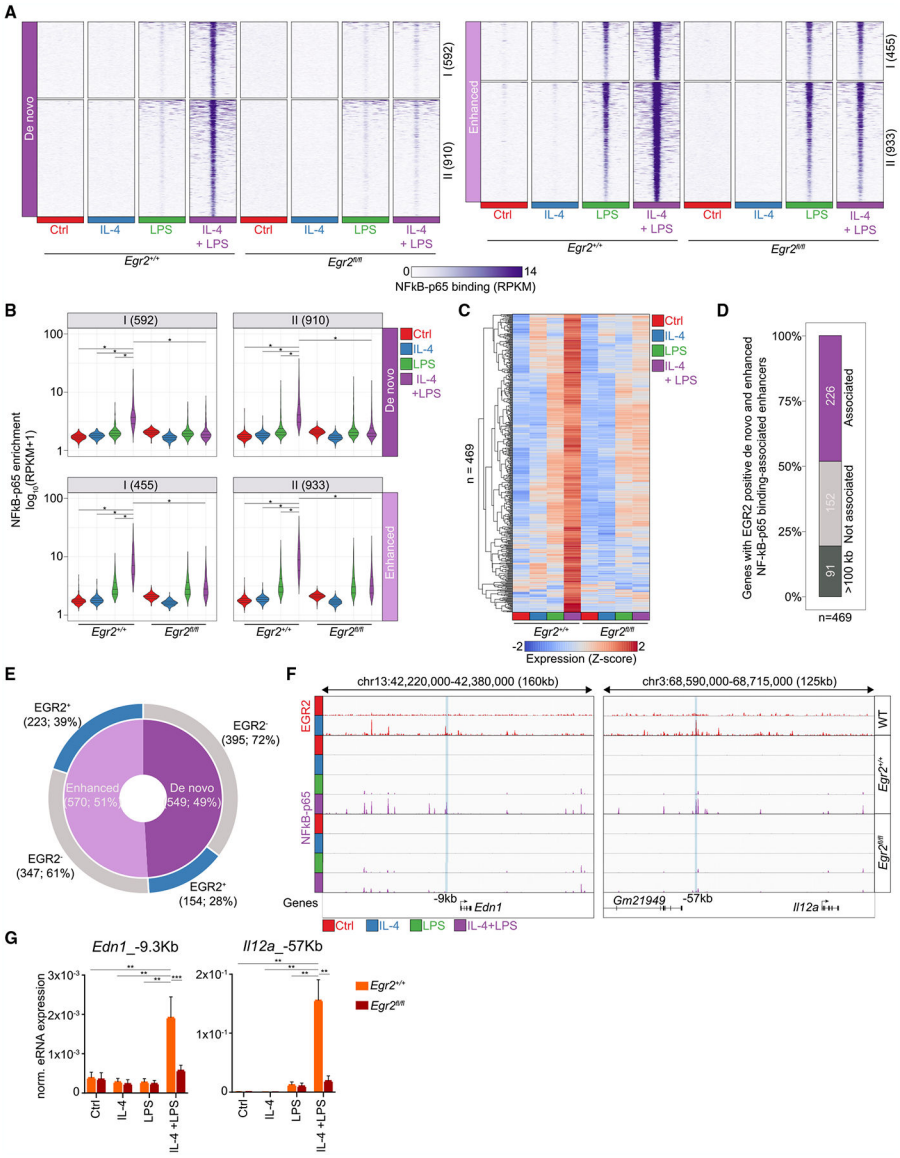

Figure 5. The IL-4-induced EGR2 transcription factor is necessary for the elevated LPS responsiveness in alternatively polarized Macs

(A) Read distribution plot visualization of NF-κB-p65 occupancy at the annotated synergistically activated *de novo* and enhanced NF-κB-p65-binding-associated regulatory regions in IL-4-primed and LPS-exposed WT (*Egr2*$^{+/+}$ *Lyz2-cre*, referred to as *Egr2*$^{+/+}$) and EGR2-deficient (*Egr2*$^{fl/fl}$ *Lyz2-cre*, referred to as *Egr2*$^{fl/fl}$) BMDMs. Results are represented in RPKM values.

(B) Average ChIP-seq signals for NF-κB-p65 are represented as violin plots on the genomic regions showing synergistic activation at *de novo* and enhanced NF-κB-p65 binding-associated genomic regions in IL-4-primed and LPS-exposed *Egr2*$^{+/+}$ and *Egr2*$^{fl/fl}$ BMDMs. Average $\log_{10}$ RPKM values are plotted. Significant changes are determined with the Wilcoxon test at $p < 0.01$.

(C) Heatmap representation of genes requiring EGR2 for synergistic activation in IL-4 primed and LPS-exposed *Egr2*$^{+/+}$ (n = 3) and *Egr2*$^{fl/fl}$ (n = 3) BMDMs.

(D) Number of synergistically activated and EGR2-dependent genes annotating with or without EGR2 positive *de novo* and enhanced NF-κB-p65 binding-associated genomic regions.

(E) The number of EGR2 positive and negative *de novo* and enhanced NF-κB-p65-binding-associated genomic regions annotating to synergistically activated and EGR2-dependent genes with a minimum of one EGR2 positive enhancer.

(F) Genome browser view on the *Il12a*, and *Edn1* loci. ChIP-seq results for EGR2 in WT and NF-κB-p65 in $Egr2^{+/+}$ and $Egr2^{fl/fl}$ Macs are shown. IL-4-primed and non-polarized Macs with or without LPS exposure are depicted for each factor.

(G) RT-qPCR measurements of eRNA expression at the selected EGR2-bound and synergistically activated enhancers from IL-4-primed and non-polarized $Egr2^{+/+}$ and $Egr2^{fl/fl}$ BMDMs following LPS exposure (n = 5 per genotype, from two independent experiments). Bar graphs present the mean ± the SD of the biological replicates. *p < 0.05, **p < 0.01, ***p < 0.001, ns, not significant change.

$Egr2^{+/+}$ and $Egr2^{fl/fl}$ bone marrow cells were isolated from mice with the C57BL/6 genetic background. BMDMs were pretreated with IL-4 for 24 h followed by LPS exposure for 1 h (A, B, and F) or for 3 h (C and G). Data in (A) and (B) are combined from two independent biological replicates per genotype.

See Figure S5.

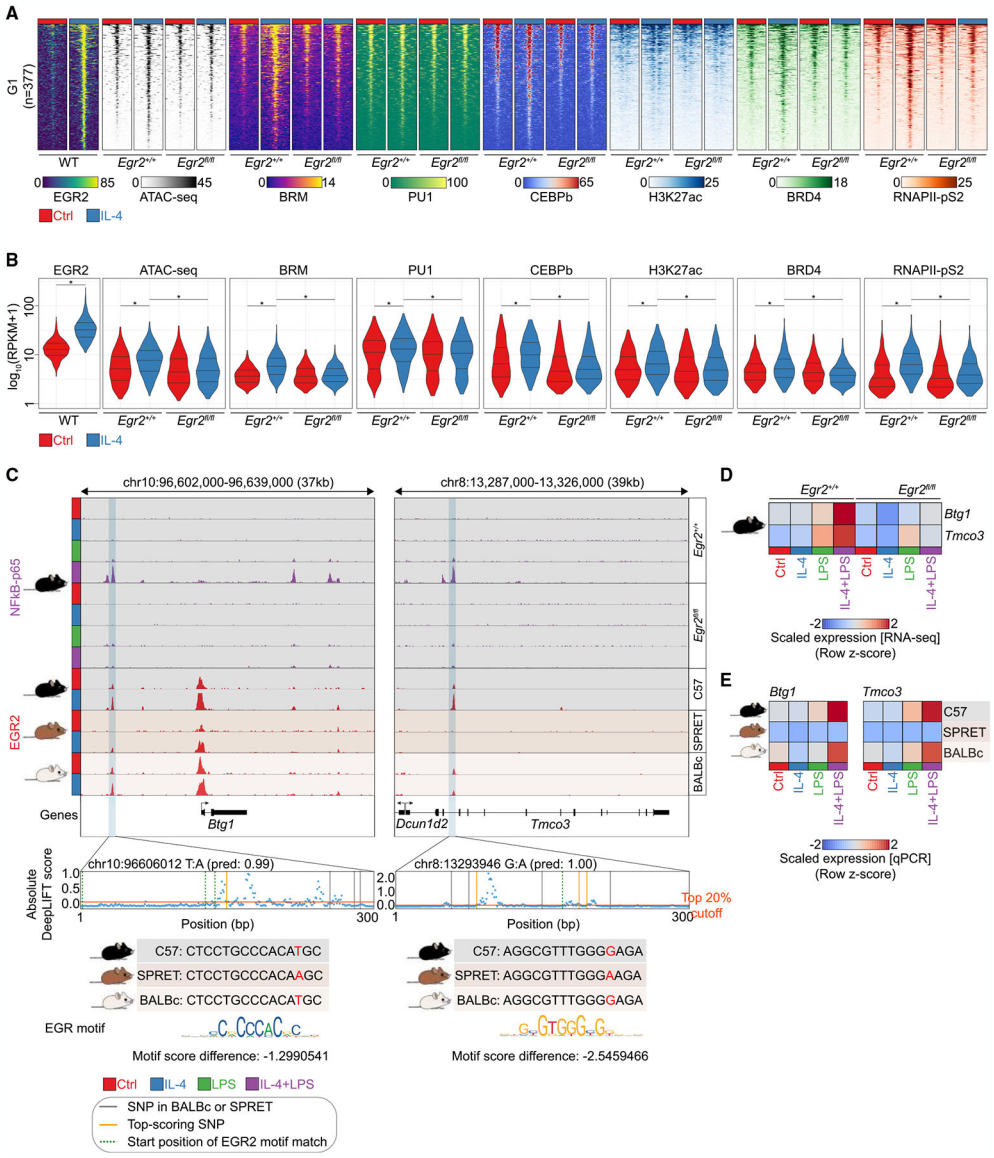

Figure 6. EGR2 binding to its response element is required for IL-4-induced epigenomic remodeling of the enhancers of highly activated genes

(A) Read distribution plot visualization of EGR2, BRM, PU.1, CEBPβ, BRD4, RNAPII-pS2 binding, H3K27Ac, and chromatin accessibility at the EGR2 positive, synergistically activated *de novo* and enhanced NF-κB-p65 binding-associated regulatory regions in IL-4-primed and non-polarized WT (*Egr2*$^{+/+}$) and EGR2-deficient (*Egr2*$^{fl/fl}$) BMDMs. Results are represented in RPKM values.

(B) Average ChIP-seq signals for EGR2, BRM, PU.1, CEBPβ, BRD4, and RNAPII-pS2 binding, H3K27Ac and ATAC-seq signals are represented as violin plots on the genomic regions showing EGR2 binding at synergistically activated *de novo* and enhanced NF-κB-p65 binding-associated genomic regions in IL-4-primed and non-polarized WT (*Egr2*$^{+/+}$) and EGR2 deficient (*Egr2*$^{fl/fl}$) BMDMs. Average $\log_{10}$ RPKM values are plotted. Significant changes are determined with the Wilcoxon test at $p < 0.01$.

(C) Genome browser view on the *Btg1* and *Tmco3* loci. ChIP-seq results for EGR2 in WT C57BL/6J (referred to as C57), SPRET/EiJ (referred to as SPRET) and BALB/cJ (referred to as BALBc) mouse strains-derived BMDMs, and NF-κB-p65 in $Egr2^{+/+}$ and $Egr2^{fl/fl}$ Macs are shown. IL-4-primed and non-polarized Macs are depicted for EGR2 and IL-4-primed and non-polarized BMDMs with or without LPS activation for NF-κB-p65. In the DeepLIFT score panels, the horizontal red lines indicate top 20% score cutoff, the vertical solid lines for genetic variations in BALBc or SPRET, and the vertical dashed lines for the start positions of EGR2 motif matches.

(D) Heatmap representation of Btg1 and Tmco3 mRNA expression in IL-4-primed and LPS-exposed $Egr2^{+/+}$ (n = 3) and $Egr2^{fl/fl}$ (n = 3) BMDMs determined by RNA-seq.

(E) Heatmap representation of *Btg1* and *Tmco3* mRNA expression in IL-4-primed and LPS-exposed WT C57, SPRET, and BALBc mouse strain-derived BMDMs determined by RT-qPCR (n = 4 per mouse strain).

$Egr2^{+/+}$ and $Egr2^{fl/fl}$ bone marrow cells were isolated from mice with C57BL/6 genetic background. BMDMs were treated with IL-4 for 24 h (A, B, and EGR2-specific ChIP-seq part of C). Additionally, BMDMs were pretreated with IL-4 for 24 h followed by LPS exposure for 1 h (NF-κB-p65-specific ChIP-seq part of C) or for 3 h (D and E). Data in (A)–(C) are combined from two independent biological replicates per genotype or mouse strain.

See Figure S6.

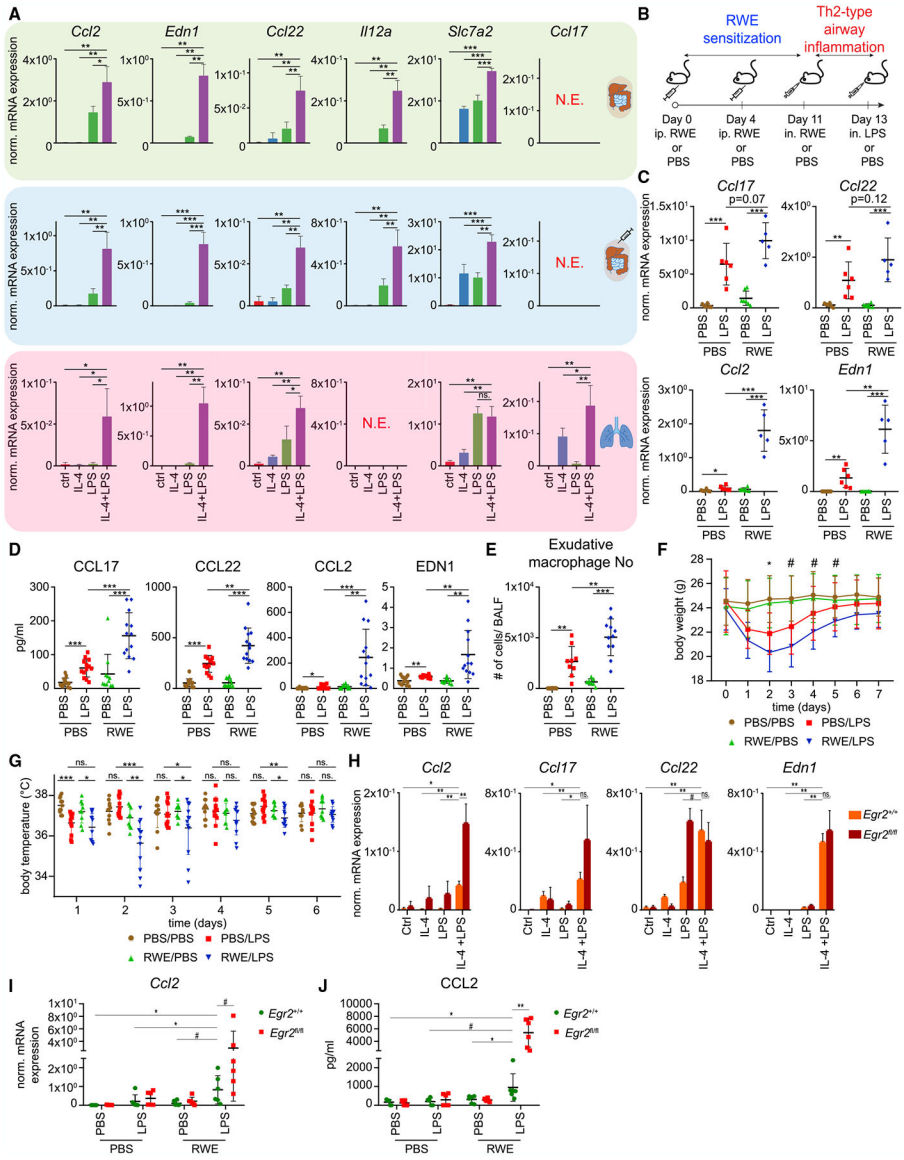

Figure 7. Extended synergy in LPS responsiveness of alveolar Macs can be observed in the murine allergic airway inflammation model

(A) RT-qPCR measurements on the indicated synergistically activated genes from IL-4-primed and non-polarized WT alveolar, resident large peritoneal, and small thioglycolate-elicited peritoneal Macs following LPS exposure (n = 4–5). Bar graphs present the mean ± SD of the biological replicates.

(B) Experimental scheme for RWE-induced Th2-type airway inflammation and intranasal LPS challenge in WT mice.

(C) RT-qPCR measurements on the indicated genes from LPS or PBS-challenged healthy and asthmatic mice-derived alveolar Macs (n = 5–6; each biological replicate was pooled from two to three animals).

(D) ELISA measurements on the indicated proteins from LPS or PBS-challenged healthy and asthmatic mice-derived bronchoalveolar lavage fluids (n = 11–13).

(E) F4/80$^+$, CD11b$^+$, and CD11c$^-$ Mac number in bronchoalveolar lavage fluid samples derived from LPS or PBS-challenged healthy and asthmatic mice (n = 8–11).
(F) LPS-induced body weight loss in control and RWE-exposed WT mice after the intranasal LPS treatment for seven consecutive days (n = 9–12).
(G) LPS-induced body temperature changes in control and RWE-exposed WT mice after the intranasal LPS treatment for 6 consecutive days (n = 9–12).
(H) RT-qPCR measurements on the indicated synergistically activated genes from IL-4-primed and non-polarized WT (*Egr2*$^{+/+}$) and EGR2-deficient (*Egr2*$^{fl/fl}$) alveolar Macs following LPS exposure (n = 3). Bar graphs present the mean ± SD of the biological replicates.
(I) RT-qPCR measurements on the LPS-induced *Ccl2* gene expression in RWE or PBS-challenged WT (*Egr2*$^{+/+}$) and Mac-specific EGR2-deficient (*Egr2*$^{fl/fl}$) mice-derived alveolar Macs (n = 5–6).
(J) ELISA measurements on the CCL2 protein in RWE or PBS-challenged WT (*Egr2*$^{+/+}$) and Mac-specific EGR2-deficient (*Egr2*$^{fl/fl}$) mice-derived bronchoalveolar lavage fluids (n = 5–6).
WT and Mac-specific EGR2-deficient mice have C57BL/6 genetic backgrounds. Alveolar and peritoneal Macs were treated with IL-4 for 24 h followed by LPS exposure for 3 h (A and H).
LPS challenge was 6 h (C, D, I, and J) or 24 h (E).
All *ex vivo* and *in vitro* experiments were repeated independently at least twice. $^{\#}p < 0.1$, $*p < 0.05$, $**p < 0.01$, $***p < 0.001$, ns, not significant change (A and C–J).
See Figure S7.

KEY RESOURCES TABLE

REAGENT or RESOURCE	SOURCE	IDENTIFIER
Antibodies		
NFκB-p65	Santa Cruz	sc-372; RRID: AB_632037
BRD4	Bethyl	A301–985A100; RRID: AB_2620184
RNAPII-pS2	Abcam	ab5095; RRID: 304749
Goat anti-Rabbit IgG (H+L) Cross-Adsorbed Secondary Antibody, Alexa Fluor™ 488	Thermo Fisher Scientific	A-11008; RRID: AB_143165
IκBα	Cell Signaling Technology	9242, RRID: AB_331623
NFκB-p65	Cell Signaling Technology	8242, RRID: AB_10859369
APC anti-mouse F4/80 Antibody	BioLegend	123116; RRID: AB_893481
PE-Cy5 anti-mouse CD11b	BioLegend	101210; RRID: AB_312793
PE-Cy7 anti-mouse CD11b	Thermo Fisher Scientific	25-0112-82; RRID: AB_469588
PE anti-mouse CD11c	BD Biosciences	561044; RRID: AB_2033996
FITC anti-mouse CD24	Thermo Fisher Scientific	11-0242-82; RRID: AB_464988
Goat-anti-mouse IgG (H+L), HRP conjugate	Advansta	R-05071–500; RRID:AB_10718209
Goat-anti-rabbit IgG (H+L), HRP conjugate	Advansta	R-05072–500; RRID:AB_10719218
Biological samples		
Short ragweed pollen extract (ambrosia artemisiifolia)	Stallergenes Greer	XP56D3A
Chemicals, peptides, and recombinant proteins		
Mouse recombinant IL-4	Peprotech	214–14
LPS (*Salmonella enterica* serotype Minnesota Re 595)	Sigma Aldrich	L6261
Mouse TLR1–9 agonist kit	Invivogen	tlrl-kit1mw
Human recombinant IL-4	Peprotech	200–04
Critical commercial assays		
High-Capacity cDNA Reverse Transcription Kit	Applied Biosystems™	4368813
Light Cycler 480 SY Green Master	Roche	4887352001
Imject™ Alum Adjuvant	Thermo Fisher Scientific	77161
CCL17/TARC ELISA Kit	R&D Systems	DY529
CCL22/MDC ELISA Kit	R&D Systems	DY439
EDN1 ELISA Kit	R&D Systems	DET100
CCL2/MCP-1	BioLegend	432704
eBioscience™ Fixable Viability Dye eFluor™ 506	Thermo Fischer Scientific	65-0866-14
Fc Receptor blocking reagent, mouse	Miltenyi Biotec	130-092-575
NEBNext Ultra II RNA Library Prep with Purification Beads	New England BioLabs	E7775S
Ovation Ultralow System V2	TECAN	0344NB-32

REAGENT or RESOURCE	SOURCE	IDENTIFIER
NextSeq 500/550 High Output Kit v2.5 (75 Cycles)	Illumina	20024906
Deposited data		
RNA-seq, NFκB-p65, RNAPII-pS2 and BRD4 ChIP-seq, ATAC-seq	This paper	GEO: GSE181223
EGR2, BRM, PU.1, H3K27Ac, BRD4 and RNAPII-pS2 ChIP-seq, ATAC-seq	Daniel et al., 2020	GEO: GSE151015
CEBPb ChIP-seq	Hoeksema et al., 2021	GEO: GSE159630
EGR2 ChIP-seq	Hoeksema et al., 2021	GEO: GSE159630
Experimental models: Cell lines		
Primary bone marrow-derived macrophages	WT C57BL/6, *Stat6*$^{-/-}$, Egr2$^{fl/fl}$ and Egr2$^{+/+}$ Lys Cre mice, WT SPRET and BALBc mice	N/A
Human CD14^{+} monocytes	Buffy coats	N/A
Experimental models: Organisms/strains		
C57BL/6	The Jackson Laboratory	N/A
SPRET	The Jackson Laboratory	N/A
BALBc	The Jackson Laboratory	N/A
Stat6$^{-/-}$	The Jackson Laboratory	N/A
Lyz2-cre	The Jackson Laboratory	N/A
Egr2$^{fl/fl}$	Prof. Patrick Charnays	N/A
Oligonucleotides		
Primers for mRNA expression	This paper	see Table S5
Primers for eRNA expression	This paper	see Table S5
Software and algorithms		
nf-core/rnaseq v3.0	Ewels et al., 2020	https://github.com/nf-core/rnaseq
nf-core/atacseq v1.2	Ewels et al., 2020	https://github.com/nf-core/atacseq
FastQC v0.11.9	–	https://www.bioinformatics.babraham.ac.uk/projects/fastqc/
STAR	Dobin et al., 2013	https://github.com/alexdobin/STAR
Salmon	Patro et al., 2017	https://github.com/COMBINE-lab/salmon
EdgeR v3.38.4	Robinson et al., 2010	https://bioconductor.org/packages/release/bioc/html/edgeR.html
DeepTools v3.5.1	Ramirez et al., 2016	https://github.com/deeptools/deepTools/tree/develop
BWA v0.7.17	Li et al., 2009	https://github.com/lh3/bwa
BEDTools v2.30.0	Quinlan and Hall, 2010	https://bedtools.readthedocs.io/en/latest/
Samtools v1.16	Li et al., 2009	http://www.htslib.org/
MACS2 v2.2.7.1	Zhang et al., 2008	https://pypi.org/project/MACS2/
HOMER v4.11	Heinz et al., 2010	http://homer.ucsd.edu/homer/index.html
DiffBind v3.6.3	Ross-Innes et al., 2012	https://bioconductor.org/packages/release/bioc/html/DiffBind.html
DESeq2 v1.36.0	Love et al., 2014	https://bioconductor.org/packages/release/bioc/html/DESeq2.html
FIMO v5.4.1	Grant et al., 2011	https://meme-suite.org/meme/tools/fimo
TOMTOM v5.4.1	Gupta et al., 2007	https://meme-suite.org/meme/tools/tomtom

REAGENT or RESOURCE	SOURCE	IDENTIFIER
JASPAR database v9	Castro-Mondragon et al., 2022	https://jaspar.genereg.net/
AgentBind v0.1	Zheng et al., 2021	https://github.com/Pandaman-Ryan/AgentBind
DeepSEA	Zhou and Troyanskaya, 2015	https://hb.flatironinstitute.org/deepsea/
DeepLIFT	Shrikumar et al. 2017	https://github.com/kundajelab/deeplift
ENCODE mm10 blacklist	Amemiya et al., 2019	https://github.com/Boyle-Lab/Blacklist
IGV v2.14.0	Robinson et al., 2011	https://software.broadinstitute.org/software/igv/
R v4.2.1	R Core Team, 2020	https://www.r-project.org/
Tidyverse v1.3.2	Wickham et al., 2019	https://github.com/tidyverse/tidyverse